

# Variational operator learning: A unified paradigm for training neural operators and solving partial differential equations

Tengfei Xu<sup>1</sup>, Dachuan Liu<sup>1</sup>, Peng Hao <sup>\*1</sup>, and Bo Wang<sup>1</sup>

<sup>1</sup>State Key Laboratory of Structural Analysis, Optimization and CAE Software for Industrial Equipment, Department of Engineering Mechanics, Dalian University of Technology, Dalian 116024, China

## Abstract

Based on the variational method, we propose a novel paradigm that provides a unified framework of training neural operators and solving partial differential equations (PDEs) with the variational form, which we refer to as the variational operator learning (VOL). We first derive the functional approximation of the system from the node solution prediction given by neural operators, and then conduct the variational operation by automatic differentiation, constructing a forward-backward propagation loop to derive the residual of the linear system. One or several update steps of the steepest decent method (SD) and the conjugate gradient method (CG) are provided in every iteration as a cheap yet effective update for training the neural operators. Experimental results show the proposed VOL can learn a variety of solution operators in PDEs of the steady heat transfer and the variable stiffness elasticity with satisfactory results and small error. The proposed VOL achieves nearly label-free training. Only five to ten labels are used for the output distribution-shift session in all experiments. Generalization benefits of the VOL are investigated and discussed.

## 1 Introduction

Solving partial differential equations (PDEs) has widespread applications in science and engineering. Conventional solvers based on a variety of classical numerical approaches (e.g., finite element methods (FEMs) [1], finite volume methods (FVMs) [2], finite difference methods (FDMs) [3], meshfree methods (MFMs) [4]) have been developed and achieve great achievements in the last decades, and they can give solutions that meet engineering accuracy requirements under appropriate settings. Commercial software developed on the basis of these conventional solvers has been used extensively in engineering. However, the conventional solvers cannot learn knowledge or experience from their history of solving previous problems, which means they have to solve a new problem from scratch each time, even if it is highly similar to the ones they have solved before. The limitation leads to heavy computational costs in scenarios that require multiple simulations of different parameters, such as inverse problems, optimum design and uncertainty quantification. With the current rapid development of deep learning algorithm, software and hardware, training neural networks to learn the solution *operator* rather than learn a specific solution function to PDEs becomes a promising way to break through the limitation of the conventional solver. But the training process of neural networks requires often a number of labels as ground truth data, which can be scarce and expensive to obtain. Thus, methods [5, 6, 7, 8, 9, 10, 11, 12] (See Table 1 for details.) that embed domain knowledge like physical laws

---

\*Corresponding author: haopeng@dlut.edu.cn

and principles into the neural network are developed, making the training process very label-efficient, even label-free. Like the classical numerical approaches that solve PDEs with different forms, these techniques also deal with different forms of PDEs: the differential form (the strong form), the equivalent integral form, the variational form (the weak form) and the functional form (See Fig. 1 and Table 1). Compared to the strong form, the weak form reduces the requirements of continuity of the solution, leading to the *weak solution*. The weak form is important for solving PDEs. First, the weak form turns the differential equations into integral equations, and lowers the order of derivatives of variables being solved, thus reducing the difficulty of solving. Second, the weak form is less strict and more robust than the strong form, and it is appropriate for describing many of the real-world phenomena with non-smooth and even discontinuous physics, such as the cracks and defects in the solid, the turbulence and shock wave in the fluid. Third, many powerful classical numerical approaches, especially FEMs and FVMs, are based on the weak form, and they have developed mature mechanisms for handling boundary conditions and determining convergence of solutions. Embedding the weak form with these well-developed mechanisms in deep neural networks can help us overcome some of the difficulties like boundary condition management [13] encountered in the strong form embedding.

Combining operator learning model and the specific domain knowledge, especially the weak form of PDEs, will lead to new numerical approaches suitable for solving parameterized PDEs. From Table 1, we observe two such combinations, which are physics-informed DeepONet (PI-DeepONet) [11] and physics-informed neural operator (PINO) [12]. However, both of them are based on the strong form of PDEs. There is a lack of research on combining the weak form and the operator learning. Combining operator learning and the weak form of PDEs deserves attention and is worth exploring. Motivated by the importance of the weak form, we marry the idea of operator learning and the weak form of PDEs with state-of-the-art neural operators and the variational method in this work.

**Our contributions.** In this paper, we propose the variational operator learning (VOL), a novel paradigm that combines training neural operators and solving partial differential equations with the variational form. The proposed VOL can nearly label-free train the Fourier neural operators (FNO [14]) and the implicit Fourier neural operators (IFNO [15]), that are two of the state-of-the-art neural operators. The distribution-shift session of the output of neural operators (See section 3.3 for more details.), which also exists in the conventional data-driven paradigm in previous works [14, 15], is the only part of the process that requires labels (Only five to ten labels are used in our experiments for the distribution-shift session.) in all procedures of the proposed VOL. To the best of the authors’ knowledge, this is the first study that applies the variational method to the label-free training of neural operators, also the first study to train neural operators with the weak form of PDEs. The main contributions of this work are summarized as follows:

- A functional approximation with the node solution and the parameters of PDEs is derived and implemented with the tensor engine of deep learning. The variational operation is implemented with automatic differentiation. Thus a forward-backward propagation loop between the node solution and the functional approximation is developed, allowing calculating the residual of the system (i.e., calculating Eq. 21.) without acquiring the element stiffness and assembling the total stiffness matrix.
- Steepest decent method (SD) and conjugate gradient method (CG) are redeveloped based on the technique of constructing forward-backward propagation loops. Only one step or several update steps of SD and CG are required in one iteration of training process. The effect of these two optimization strategies with different layer settings are investigated and discussed. Experimental results show that the VOL can train neural operators on steady heat transfer and variable stiffness elasticity problems effectively with almost no labels. Five to ten labeled data are used in the distribution-shift session of

the output. No data-driven loss term that requires external labels is used in all experiments in this paper.

- We propose that *generalization* of neural operators can improve the performance of the iteration methods in the framework of the proposed VOL. In the framework of the VOL, neural operators keep learning and give better initial solutions in every iteration. Experimental results show the *generalization* mechanism of neural operators in the VOL can reduce the mean relative  $L_2$  error by an order of magnitude.

The remainder of the paper is structured as follows. In section 2, we list relevant fields with some of the representative literature to provide a rich context of our work. Specifically, we discuss conventional surrogate modeling, domain knowledge coupling, including domain knowledge embedding and deep model embedding, the concept of operator learning and neural operators. In section 3, we describe the theory and the implementation of the proposed VOL in detail. Then in section 4, numerical experiments and discussion of the experimental results are given. Finally, we draw conclusions and give an outlook on future directions of research in section 5.

## 2 Related work

**Surrogate modeling.** Surrogate modeling has been proposed to alleviate the computational burden of conventional solvers. Two main strategies, reduced order modeling methods (ROMs) and data-fit modeling methods (DFMs), have been adopted in the surrogate modeling. The main idea of these strategies is to seek a surrogate model of the original complex model so as to reduce or avoid the use of the conventional solver at the evaluation stage. ROMs [16] use limited available snapshots from the original high-fidelity computational models to build simplified ones in the space of reduced basis. The constructed reduced-order models are computationally efficient compared with original full-order models. On the other hand, DFMs [17] including response surface methods, Kriging methods and neural networks, perform interpolation or regression of parameter-response pairs sampled from the high-fidelity dataset. The popular deep learning approach can also be considered as a kind of DFMs. An enormous amount of work of deep neural networks, including the neural operators [18, 19, 9, 20, 14, 21], has focused on utilizing deep learning techniques to design excellent neural surrogate models.

Two stages are usually required for both ROMs and DFMs to get a surrogate model in a pure data-driven manner: (1) *Data preparation*. At this stage, high-fidelity labels from the simulation of the conventional solvers or real-world experiments are produced and collected. Both ROMs and DFMs require often a fair number of such expensive labels. (2) *Model construction (model training)*. Available labeled data from stage (1) are utilized to construct the surrogate model, which brings another computational cost.

It is worth noting that, despite the existence of techniques such as active learning [22] that tightly couple these two stages, they are in reality isolated from each other. The data preparation stage just provides limited labels as examples, and keeps itself a black box to the surrogate models to be trained in the whole process of simulating or experimenting. Besides, the model training stage has no influence on the solving process in the data preparation stage, for example, it cannot accelerate the convergence of solving. Models trained in such a pure data-driven fashion can only acquire knowledge indirectly through the labels. If the model can learn directly from the domain knowledge, it is possible to skip the data preparation stage, and the model training process is to a certain extent equivalent to solve the original PDEs. Two ways to help coupling the model with domain knowledge, i.e., domain knowledge embedding and surrogate model embedding, are discussed in the next paragraph.

**Domain knowledge embedding and deep model embedding.** Domain knowledge embedding is to embed domain knowledge (e.g., governing equations, discretization schemes, symmetries, variational principles) into the architecture of the (deep learning) model and training process. There are two common approaches to embed domain knowledge: (1) *Automatic differentiation*. Automatic differentiation is a powerful tool to calculate derivatives in deep learning. The derivatives of the output with respect to input parameters such as spatial coordinates and time, the Jacobian matrix, and even the Hessian matrix can be easily obtained with automatic differentiation. Thus, the governing equations or their weak form with derivative terms can be implemented elegantly in deep learning. Here we list some representative research that uses automatic differentiation to implement domain knowledge embedding. Deep Ritz method [5] constructs a functional with automatic differentiation and numerical integration, and sets the minimization objective as the functional. Deep Galerkin method (DGM) [6] and physics-informed neural network (PINN) [7] are very similar, both of which use the residual error of the strong form, i.e., the original governing equations, and derive it with automatic differentiation, besides, both of the methods treat the boundary conditions as penalty terms. (2) *Discretization*. Discretization technique is a much broader topic. Some research including PhyGeoNet [9], DiscretizationNet [10] discretizes the output of the deep learning model with finite difference or finite volume discretization schemes to approximate derivative terms in the governing equations. FEA-Net [23] uses convolution kernel to express stiffness feature of the structure discretized by finite elements. Motivated by the domain knowledge of the multigrid algorithm, a deep neural architecture called MgNet [24] is designed and successfully used in dataset CIFAR-10 and CIFAR-100 [25] for image classification.

In contrast to domain knowledge embedding, deep model embedding is to embed the deep learning model in the classical numerical approach. Deep potential [26] leverages deep neural network representation of the potential energy surface for atoms and molecules system, which is a promising alternative to the classical potential representation in molecular dynamics and Monte Carlo simulations. Problem-independent machine learning [27] embeds a simple feedforward neural network in the framework of extended multi-scale finite element method [28] to learn the mapping between discretized material density field of the coarse element and the multi-scale numerical shape functions of the element. Deep conjugate direction method [29] uses the output of a deep convolutional neural network embedded in the algorithm to construct a good search direction which accelerates the convergence for solving large, sparse, symmetric, positive-definite linear systems. Fourier neural solver [30] embeds a neural network in the stationary iterative method to help to eliminate error components in frequency space.

In summary, domain knowledge embedding and deep model embedding do not necessarily reduce or eliminate the usage of labels, however, by marrying the domain knowledge and the deep learning models, they achieve better results than using deep learning model alone and using classical numerical approaches alone. Specifically, domain knowledge embedding can help reduce label use of deep learning models or design new neural architectures with embedding domain knowledge into the deep learning models, and deep model embedding enhances the capabilities of the the classical numerical approach by the various useful properties of the deep learning model. For both approaches, we just list some of the representative research in recent years.

**Operator learning and neural operators.** Operator learning is to let the model learn the operator between two function spaces. Operator learning models, which we say are *operator-based*, can give prediction over a whole parameter set of parameterized PDEs. Compared to *function-based* models that can only give prediction of a single parameter, operator learning models are attractive in applications like inverse problems, optimum design and uncertainty quantification. In Table 1, we classify some of the representative existing methods according to whether they are function-based or operator-based. Neural operators refer to specific neural network architectures designed for operator learning. According to the type of input and output

of the neural networks, the existing architectures of neural operators can be divided into two categories: (1) *Point-wise (the family of DeepONets)*. Inspired by the universal approximation theorem for operators [31, 32], DeepONet [21] receives the parameter field and a query point, and then output solution of the query points in the solution domain. DeepONet has a branch net for encoding discrete function space, and a trunk net for encoding the coordinate information of query points, the output of DeepONet is the inner product of the output of two nets. (2) *Field-wise*. These architectures [20, 14, 15] input discrete parameter fields and output discrete solution fields. Fourier neural operators [14] parameterize the integral kernel in the Fourier space and utilize the idea of shortcut connection, producing a powerful Fourier layer. The implicit Fourier neural operator [9] utilizes the Fourier layer in an implicit manner, which lets the data flow pass through the Fourier layer recurrently and has better training stability. It is worth noting that, in addition to the neural operators that are specifically designed for operator learning, the idea of operator learning has also been practiced with other neural architectures, like the convolutional neural network (CNN) [18] and the generative neural network (GAN) [19].

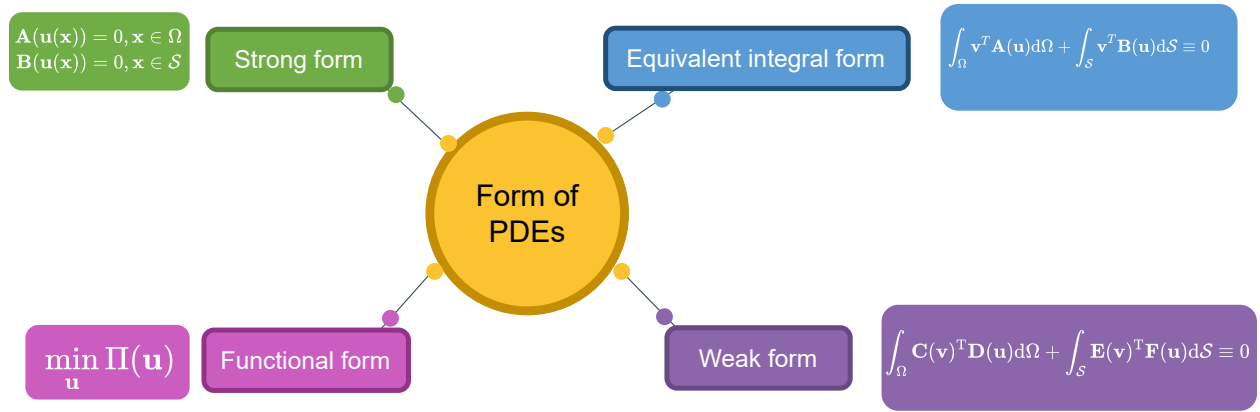


Figure 1: Different forms of PDEs.

### 3 Variational operator learning (VOL) algorithm

In this section, the variational operator learning (VOL) algorithm is developed. The VOL does not create any novel neural operator architecture, instead, it focuses on training the existing state-of-the-art neural operators with the smallest possible amount of labeled data, even no label. Generalization of deep learning makes the training (also solving) process efficient: while learning and solving a batch of samples, the VOL can improve the potential performance on other samples. The overall process of the VOL is shown in Fig. 3. In section 3.1, a general setting of elasticity is chosen, as the background to derive the principle of virtual work as a variational form of the governing equations. And the formulation of the functional of the continuum elastic system is given. In section 3.2, the approximation of functional used by VOL is derived, and the optimization objective of VOL is constructed.

#### 3.1 Problem settings

Consider a linear elastic body  $\mathcal{B} \subset \mathbb{R}^3$  (Fig. 2). Let the boundary of the body be  $\mathcal{S} = \mathcal{S}_{\sigma} \cup \mathcal{S}_u$ , where  $\mathcal{S}_{\sigma}$  is the traction boundary, and  $\mathcal{S}_u$  is the displacement boundary. Let the interior of the body be  $\Omega$ . The

	Function-based		Operator-based		Type of methods		Form of PDEs			
	Classical numerical approach		Data-driven modeling		Domain knowledge embedding		Differential form	Equivalent Integral Form	Functional form	Variational form
Analytical methods	✓						✓			
FDMs	✓		✓				✓			
Weighted residual methods	✓		✓					✓		
Ritz method	✓		✓							✓
FEMs	✓		✓							✓
FVMs	✓		✓							✓
ROMs				✓						
Deep Ritz method [5]	✓		✓						✓	
DGM [6]	✓				✓		✓			
PINN [7]	✓				✓		✓			
Literature [8]	✓				✓				✓	
PhyGeoNet [9]					✓		✓			
DiscretizationNet [10]	✓				✓					✓
DeepONet [21]			✓							
ENO [14]			✓							
PI-DeepONet [11]			✓		✓		✓			
PINO [12]			✓		✓		✓			
<b>VOL (ours)</b>			✓		✓					✓

Table 1: Summary of some of the representative existing methods in the field of solving PDEs and approximating solutions to PDEs.

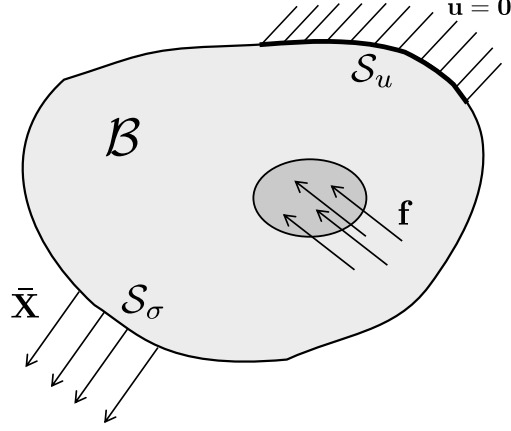


Figure 2: A linear elastic body with body forces and boundary conditions.

governing equations and boundary conditions of  $\mathcal{B}$  are

$$\begin{cases} \sigma_{ij,j} + f_i = 0, & \text{in } \Omega \\ \bar{X}_i = \sigma_{ij}n_j, & \text{on } S_\sigma \end{cases} \quad (1)$$

where  $\sigma = [\sigma_{ij}]$  is the stress tensor,  $\mathbf{f} = [f_i]$  are the body forces, and  $\bar{\mathbf{X}} = [\bar{X}_i]$  are the traction forces. The weighted integral form of Eq. 1 is

$$\begin{aligned} \int_{\Omega} (\sigma_{ij,j} + f_i) \delta u_i d\Omega + \int_{S_\sigma} (\bar{X}_i - \sigma_{ij}n_j) \delta u_i dS &= 0 \\ \forall \delta u_i \in \{v \in C[\Omega]; v = 0, \text{ on } S_u\} \end{aligned} \quad (2)$$

and note

$$\begin{aligned} \int_{\Omega} \sigma_{ij,j} \delta u_i d\Omega - \int_{S_\sigma} \sigma_{ij}n_j \delta u_i dS &= \int_{\Omega} \sigma_{ij,j} \delta u_i d\Omega - \int_S \sigma_{ij}n_j \delta u_i dS = - \int_{\Omega} \sigma_{ij} \delta u_{i,j} d\Omega \\ &= - \int_{\Omega} \frac{1}{2} \sigma_{ij} (\delta u_{i,j} + \delta u_{j,i}) d\Omega = - \int_{\Omega} \sigma_{ij} \delta \varepsilon_{ij} d\Omega \end{aligned} \quad (3)$$

where  $\varepsilon = [\varepsilon_{ij}]$  is the strain tensor. Substituting Eq. 3 into Eq. 2, we have

$$\begin{aligned} \int_{\Omega} f_i \delta u_i d\Omega + \int_{S_\sigma} \bar{X}_i \delta u_i dS &= \int_{\Omega} \sigma_{ij} \delta \varepsilon_{ij} d\Omega \\ \forall \delta u_i \in \{v \in C[\Omega]; v = 0, \text{ on } S_u\} \end{aligned} \quad (4)$$

Eq. 4 is also known as *the principle of virtual work*, which is a variational form of Eq. 1. The left term of Eq. 4 is the virtual work done by the external forces, and the right term is the strain energy of the elastic body  $\mathcal{B}$  (also the opposite of the virtual work done by the internal forces). Thus, we have

$$\delta W_{\text{int}} + \delta W_{\text{ext}} = -\delta [U + U_e] = 0 \quad (5)$$

where  $\delta W_{\text{int}}$ ,  $\delta W_{\text{ext}}$  are the virtual work done by the internal forces and the virtual work done by the external forces respectively.  $U$  is the strain energy of the elastic body  $\mathcal{B}$ , and  $U_e$  is the potential energy of the external forces. Let the functional of the system be  $\Pi$ , and we have

$$\begin{aligned} \delta \Pi &= 0 \\ \Pi &= U + U_e \\ \forall \delta u_i \in \{v \in C[\Omega]; v = 0, \text{ on } S_u\} \end{aligned} \quad (6)$$

Note Eq. 6 is equivalent to Eq. 1, and here we only give the derivation of Eq. 6 from Eq. 1.

For convenience, we rewrite the stress tensor and strain tensor in their vector form, i.e.,

$$\boldsymbol{\sigma} = [\sigma_x, \sigma_y, \sigma_z, \tau_{yz}, \sigma_{xz}, \sigma_{xy}]^T, \boldsymbol{\varepsilon} = [\varepsilon_x, \varepsilon_y, \varepsilon_z, \tau_{yz}, \varepsilon_{xz}, \varepsilon_{xy}]^T$$

Then the strain energy of the elastic body and the potential energy of the external forces is

$$\begin{aligned} U &= \int_{\Omega} \frac{1}{2} \boldsymbol{\varepsilon}^T \mathbf{C} \boldsymbol{\varepsilon} d\Omega \\ U_e &= - \int_{\Omega} \mathbf{f}^T \mathbf{u} d\Omega - \int_{S_{\sigma}} \bar{\mathbf{X}}^T \mathbf{u} dS \end{aligned} \quad (7)$$

Thus, functional  $\Pi$  is:

$$\Pi = U + U_e = \int_{\Omega} \frac{1}{2} \boldsymbol{\varepsilon}^T \mathbf{C} \boldsymbol{\varepsilon} d\Omega - \int_{\Omega} \mathbf{f}^T \mathbf{u} d\Omega - \int_{S_{\sigma}} \bar{\mathbf{X}}^T \mathbf{u} dS \quad (8)$$

where  $\mathbf{C}$  is the matrix of material properties. Note  $\Pi$  is the total potential energy of the system.

In context of operator learning, for example,  $\mathbf{C}$  can be a function of coordinates  $\mathbf{C}(x, y, z)$  in random function spaces, and our goal is to learn an operator learning model, which outputs the displacement field  $\mathbf{u}$  that lets  $\delta\Pi = 0$  hold as close as possible for each input instance with  $\mathbf{C}(x, y, z)$  in the test set. For steady heat transfer problems, we can also write the functional of the system (See Eq. 30 in section 4.2.).

### 3.2 Functional approximation and variational operation

In this section, we construct an approximation of the system functional for the VOL, i.e., to seek the approximation of Eq. 8, the formulation of which is a bit different from that in FEMs, making it possible to approximate functional without calculating stiffness matrices. The optimization objective is then established by variational operation. It is worth noting that it is possible for the VOL to use various discretization scheme, notwithstanding the VOL uses the same discretization scheme (piecewise polynomial interpolation) as FEMs in this paper:

$$\begin{aligned} \mathbf{u}(x, y, z) &= \mathbf{N}(r, s, t) \mathbf{a}^e \\ \mathbf{x} &= \mathbf{N}(r, s, t) \mathbf{x}^e \end{aligned} \quad (9)$$

where  $\mathbf{u}(x, y, z)$  denotes the displacement of at point  $\mathbf{x} = (x, y, z)$  in the physical coordinate system, and also the point  $\mathbf{r} = (r, s, t)$  in the parameter coordinate system,  $\mathbf{a}^e$  denotes the displacement vector of nodes of the element, and  $\mathbf{N}$  denotes shape function matrix of the element. Note  $\mathbf{u}(x, y, z)$  and  $\mathbf{a}^e$  are node-related quantities, they can represent the displacement in the context of solid mechanics, and the temperature in heat transfer, etc.

We take an elastic body discretized by isoparametric elements as an example. In this case, the node solution is the node displacement tensor of the elastic body. The classical expression of functional approximation in FEMs is:

$$\begin{aligned} \tilde{\Pi} &= \sum_e \Pi^e = \frac{1}{2} \sum_e \left( \mathbf{a}^{eT} \int_{\Omega_e} \mathbf{B}^T \mathbf{D} \mathbf{B} d\Omega \mathbf{a}^e \right) \\ &\quad - \sum_e \left( \mathbf{a}^{eT} \int_{\Omega_e} \mathbf{N}^T \mathbf{f} d\Omega \right) - \sum_e \left( \mathbf{a}^{eT} \int_{S_{\sigma}^e} \mathbf{N}^T \bar{\mathbf{X}} dS \right) \end{aligned} \quad (10)$$

where  $\tilde{\Pi}$  denotes the approximation of  $\Pi$  in Eq. 8,  $\mathbf{B}$  denotes strain-displacement matrix of the element, and  $\mathbf{D}$  denotes elastic constitutive matrix, which is just another mark of  $\mathbf{C}$  in Eq. 8. The  $\int_{\Omega_e} \mathbf{B}^T \mathbf{D} \mathbf{B} d\Omega$ ,



$\int_{\Omega_e} \mathbf{N}^T \mathbf{f} d\Omega$  and  $\int_{S_\sigma^e} \mathbf{N}^T \bar{\mathbf{X}} dS$  in Eq. 10 are element stiffness matrix, element volume load vector and element face load vector respectively. If we note

$$\begin{aligned} \mathbf{K}^e &= \int_{\Omega_e} \mathbf{B}^T \mathbf{D} \mathbf{B} d\Omega \\ \mathbf{P}^e &= \int_{\Omega_e} \mathbf{N}^T \mathbf{f} d\Omega + \int_{S_\sigma^e} \mathbf{N}^T \bar{\mathbf{X}} dS \end{aligned} \quad (11)$$

and let  $\mathbf{G}^e$  be node index mapping matrix between the element and the global structure, we have

$$\tilde{\Pi} = \frac{1}{2} \mathbf{a}^T \sum_e (\mathbf{G}^{eT} \mathbf{K}^e \mathbf{G}^e) \mathbf{a} - \mathbf{a}^T \sum_e (\mathbf{G}^{eT} \mathbf{P}^e) \quad (12)$$

and

$$\mathbf{K} = \sum_e \mathbf{G}^{eT} \mathbf{K}^e \mathbf{G}^e \quad \mathbf{P} = \sum_e \mathbf{G}^{eT} \mathbf{P}^e \quad (13)$$

where  $\mathbf{K}$  is the global stiffness matrix,  $\mathbf{P}$  is the global load vector.

In FEMs, element stiffness matrices in Eq. 11 are obtained by numerical integration and then are assembled together with Eq. 13 to form the global stiffness matrix. On the other hand, the VOL solves PDEs without calculating any stiffness matrices, which is elaborated in the following paragraphs. The formulation of element stiffness matrix given by Gaussian quadrature method is:

$$\mathbf{K}^e = \int_{\Omega_e} \mathbf{B}^T \mathbf{D} \mathbf{B} d\Omega \approx \sum_{l=1}^{n_g} H_l \mathbf{B}_l^T \mathbf{D}_l \mathbf{B}_l |\mathbf{J}_l^e| \quad (14)$$

where  $n_g$  denotes the number of Gauss points of the element volume,  $H_l$  is the weight of the  $l$ th Gauss point, and  $\mathbf{J}^e$  denotes the Jacobian matrix of the element. The subscript " $l$ " denotes that the value is taken at the  $l$ th Gauss point. Similarly,

$$\mathbf{P}^e \approx \sum_{l=1}^{n_g} H_l \mathbf{N}_l^T \mathbf{f}_l |\mathbf{J}_l^e| + \sum_{m=1}^{n_{S_\sigma^e}} \sum_{l=1}^{n_m} I_{ml} \mathbf{N}_{ml}^T \bar{\mathbf{X}}_{ml} \left| \mathbf{J}_{ml}^{S_\sigma^e} \right| \quad (15)$$

where  $n_{S_\sigma^e}$  denotes the number of the faces of the element,  $n_m$  denotes the number of Gauss points of the  $m$ th face of the element,  $I_{ml}$  denotes the weight of the  $l$ th Gauss point of the  $m$ th face of the element, and  $\mathbf{J}_{ml}^{S_\sigma^e}$  denotes the Jacobian matrix of  $m$ th face of the element. The subscript " $ml$ " denotes that the value is taken at the  $l$ th Gauss point of the  $m$ th face of the element. Substitute Eq. 14, Eq. 15 into Eq. 10, and note

$$\boldsymbol{\varepsilon} = \mathbf{B} \mathbf{a}^e \quad (16)$$

Then we have another kind of formulation to express the functional, which is slightly different from Eq. 10 and Eq. 12:

$$\begin{aligned} \tilde{\Pi} &= \sum_e \Pi^e \approx \frac{1}{2} \sum_e \sum_{l=1}^{n_g} H_l \mathbf{a}^{eT} \mathbf{B}_l^T \mathbf{D}_l \mathbf{B}_l \mathbf{a}^e |\mathbf{J}_l^e| \\ &\quad - \sum_e \sum_{l=1}^{n_g} H_l \mathbf{a}^{eT} \mathbf{N}_l^T \mathbf{f}_l |\mathbf{J}_l^e| - \sum_e \sum_{m=1}^{n_{S_\sigma^e}} \sum_{l=1}^{n_m} I_{ml} \mathbf{a}^{eT} \mathbf{N}_{ml}^T \bar{\mathbf{X}}_{ml} \left| \mathbf{J}_{ml}^{S_\sigma^e} \right| \end{aligned} \quad (17)$$

or

$$\begin{aligned} \tilde{\Pi} &= \sum_e \Pi^e \approx \frac{1}{2} \sum_e \sum_{l=1}^{n_g} H_l \boldsymbol{\varepsilon}_l^T \mathbf{D}_l \boldsymbol{\varepsilon}_l |\mathbf{J}_l^e| \\ &\quad - \sum_e \sum_{l=1}^{n_g} H_l \mathbf{a}^{eT} \mathbf{N}_l^T \mathbf{f}_l |\mathbf{J}_l^e| - \sum_e \sum_{m=1}^{n_{S_\sigma^e}} \sum_{l=1}^{n_m} I_{ml} \mathbf{a}^{eT} \mathbf{N}_{ml}^T \bar{\mathbf{X}}_{ml} \left| \mathbf{J}_{ml}^{S_\sigma^e} \right| \end{aligned}$$

The VOL uses formulations like Eq. 17 to approximate functional, while FEMs use Eq. 10 or Eq. 12. It is clear that neither the element stiffness matrix nor the global stiffness matrix appears in Eq. 17. Thus, to calculate Eq. 17, the calculation and the assembly process of the element stiffness matrices can be simply skipped. In section 3.3, Eq. 17 is implemented in deep learning tensor operation. The same technique is also used in optimization strategies for the VOL, which is elaborated in section 3.3.

According to Eq. 6 and Eq. 9, the node solution field should satisfy

$$\delta\tilde{\Pi} = \frac{\partial\tilde{\Pi}}{\partial a_1}\delta a_1 + \frac{\partial\tilde{\Pi}}{\partial a_2}\delta a_2 + \cdots + \frac{\partial\tilde{\Pi}}{\partial a_{n_f}}\delta a_{n_f} = 0 \quad (18)$$

Eq. 18 is also called the *stationary condition* of  $\tilde{\Pi}$ , where  $n_f$  denotes the total number of degrees of freedom of all nodes in the computational mesh. Since  $\delta a_1, \delta a_2, \cdots, \delta a_{n_f}$  are the virtual displacement of nodes, we have

$$\frac{\partial\tilde{\Pi}}{\partial \mathbf{a}} = \mathbf{0} \quad (19)$$

Substituting Eq. 12 and Eq. 13 into Eq. 19, we have

$$\mathbf{K}\mathbf{a} = \mathbf{P} \quad (20)$$

FEMs approximate the functional (Eq. 12), perform variational operation (Eq. 19) *offline*, form and solve Eq. 20 *online*. On the other hand, the VOL approximates the functional (Eq. 17) and performs the variational operation *online* after every forward propagation. The VOL performs the variational operation to get the residual  $\mathbf{R}$  of the predicted node solution field:

$$\mathbf{R} = \frac{\partial\tilde{\Pi}}{\partial \mathbf{a}} = \mathbf{K}\mathbf{a} - \mathbf{P} \quad (21)$$

The optimization objective of VOL is to find parameters of the neural operator that minimize the average of residual norm of the whole label-free training set:

$$\begin{aligned} \min_{\mathbf{a}_i} \quad & \frac{1}{D} \sum \|\mathbf{R}_i\|_{i=1}^D \\ \text{s.t.} \quad & \mathbf{R}_i = \mathbf{K}\mathbf{a}_i - \mathbf{P} \end{aligned} \quad (22)$$

For implementation, the residual  $\mathbf{R}$  is treated as a tensor. Thus, we just calculate the norm of the flattened  $\mathbf{R}$  as the residual norm.

The Deep Ritz method [5] and the literature [8] also construct the functional of the system, but they just simply set direct functional minimization as the goal of optimization, that is, they treat the functional as the loss function in deep learning pipeline. Our approach goes a step further. Rather than minimize the functional directly, we choose to set minimizing the norm of residual that derived from the variational operation as the optimization objective. Besides, we do not set the norm of the residual itself as the loss function, but turn to solve the corresponding linear system by utilizing the connection between the computational mesh, the residual and the linear system to minimize the norm of the residual. See Fig. 7 and the next section for more details.

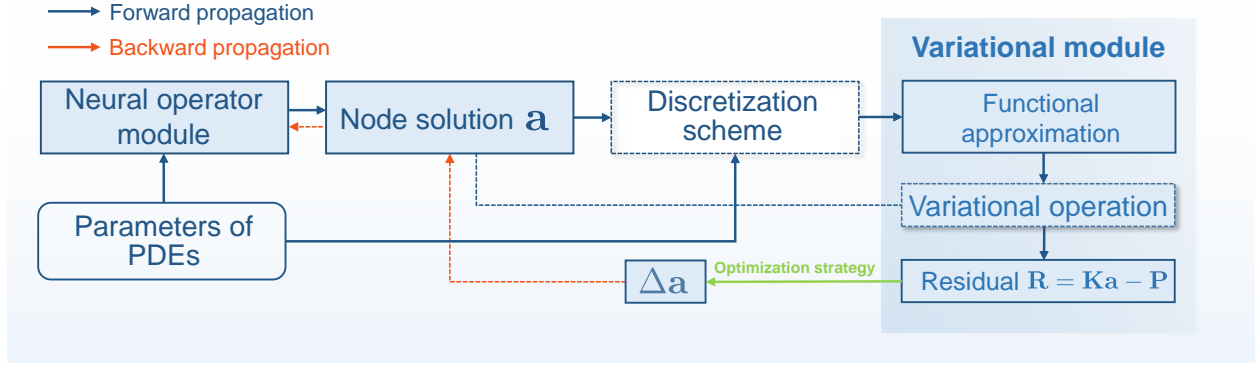


Figure 3: **The framework of variational operator learning (VOL).** The main operations, modules, and a forward and a backward propagation process of the VOL are illustrated.

### 3.3 Implementation details

---

#### Algorithm 1 Stochastic gradient decent for the VOL

---

**Input:** neural operator module  $\mathcal{N}_{operator}(\theta)$ , number of epochs  $N$ , optimization strategy  $Opt$ , learning rate  $\eta$ , and label-free training set  $\mathcal{D}=\{\mathbf{U}_i\}_{i=1}^D$ , max iteration number of one epoch  $maxiter$ , mask operation  $Mask$ , Shift set  $Shift$

- 1: **for**  $1 \leq i \leq N$  **do**
- 2:   **for**  $1 \leq j \leq maxiter$  **do**
- 3:     Sample a minibatch of  $bs$  examples  $\mathbf{U}_j^{bs}$  from  $\mathcal{D}$
- 4:      $\mathbf{a}_j^{bs} = \mathcal{N}_{operator}(\theta)(\mathbf{U}_j^{bs}, Mask, Shift)$
- 5:     Calculate total  $\tilde{\Pi}_j$  corresponding to  $(\mathbf{U}_j^{bs}, \mathbf{a}_j^{bs})$
- 6:      $\mathbf{R}_j^{bs} = \frac{\partial \tilde{\Pi}_j}{\partial \mathbf{a}_j^{bs}}$
- 7:      $\mathbf{R}_j^{bs} = Mask(\mathbf{R}_j^{bs})$
- 8:      $\Delta \mathbf{a}_j^{bs} = Opt(\mathbf{R}_j^{bs}, \mathbf{a}_j^{bs}, \mathbf{U}_j^{bs}, Mask)$
- 9:      $\theta = \theta + \eta \cdot \text{einsum}(' \cdots \mathbf{t}, \cdots -> \mathbf{t}', \text{grad}(\mathbf{a}_j^{bs}, \theta), \Delta \mathbf{a}_j^{bs})$
- 10:   **end for**
- 11: **end for**

**Return:** learned neural operator module  $\mathcal{N}_{operator}(\theta)$

---

The proposed VOL can be seamlessly integrated into deep learning training pipeline. In this paper, we embed the proposed VOL into stochastic gradient decent (SGD), a widely used algorithm in training of deep neural networks, as shown in Algorithm 1. The Algorithm 1 demonstrates a complete training process including the outer epoch loop and the inner dataset loop. Here we just start discussion at the inner loop.

Line 4 of the Algorithm 1 shows a standard forward propagation from unlabeled input parameters to the node solution. Each channel of the node solution tensor contains a certain component of the node solution. The number of the channels of the node solution tensor equals to the number of components of the solution of the PDEs. In this work, the Fourier neural operator (FNO) [14] and implicit Fourier neural operator (IFNO) [15] are used in the neural operator module with moderate modification. Related network details is shown

in Fig. 4. For the parameter tensor, parameters of PDEs are first discretized at Gauss points, and then are aggregated into the parameter tensor. Parameters at Gauss points that at the same position of all elements are encoded into one channel of the parameter tensor. Thus, the number of the channel of the parameter tensor equals to number of Gauss points in one element, as shown in Fig. 5A. The alignment operation adjusts the parameter tensor that originally discretized at Gauss points to discretization at nodes, which is implemented with the transposed convolution, as shown in Fig. 5B. Then, the lifting layer lifts the tensor to a higher channel space.  $N$  Fourier layers are adopted, and the process of data passing Fourier layers can be either explicit (FNO) or implicit (IFNO)<sup>1</sup>. Then, the projection layer projects tensor to the solution space. Two additional operations are performed on the output of neural operators. (1) Mask operation. The mask operation is designed to apply the essential boundary condition such as displacement boundary condition in elasticity and temperature boundary condition in heat transfer to the system, which is equivalent to the constraint imposition process in the FEMs. First, a mask tensor that contains 0 and 1 is constructed, which has the same shape as the node solution. Every element in the mask tensor corresponds to a certain degree of freedom of a certain node in the computational mesh. If a element of the mask tensor is "0", it means that the corresponding degree of freedom of the corresponding node is constrained, while "1" means not constrained. Then, the element-wise product between the solution tensor and the mask tensor is calculated, as shown in Fig. 6. The technique of the mask operation can be categorized into the so-called *hard* manners that used in literature [33, 9] to enforce the boundary condition of PDEs, which is different to the *soft* manner, where the BCs are treated as penalty terms in the loss function. The mask operation can also be extended to the inhomogeneous case. As shown in Fig. 6, we simply add a shift tensor with the same shape after the element-wise product operation, the elements of which are 0 where the corresponding elements of the mask tensor are 1 (unconstrained), and the other elements are the inhomogeneous terms of constraints. (2) Distribution-shift. This operation that exists in the work FNO [14] and IFNO [15] is remained in this work. It first computes the mean *mean* and the standard deviation *std* of all labels of the training set, and then use the following equation to shift the output of the neural operators to the distribution of the labels:

$$output = output \otimes std + mean \quad (23)$$

Such a shift operation can stabilize the training process. In this work, however, since the training set contains no labels (To emphasize this, the training set is also called the *label-free training set*.), additional parameters of PDEs are randomly sampled and then labeled by the commercial CAE software. These labeled data are only used in the distribution-shift session, and not used in the formal training process. We call these labeled data the *shift set*. We do not use any data-driven loss term that requires external labels in our training process for all experiments in this work.

For line 5 of Algorithm 1, to conduct numerical integration and get the functional approximation of Eq. 17 in the forward propagation of the VOL, given discrete node solution field, all terms need to be evaluated at every Gauss points, and finally be accumulated together. Such a process needs four steps (Fig. 8A to Fig. 8D):

(1) Calculate the weighted sum of node-related physical quantities weighted by the interpolation function and its spatial derivatives at Gauss points. Observe Eq. 9, the left term of which can be seen as the weighted sum of node-related physical quantities  $\mathbf{a}^e$ :

$$u_i = \sum_{j=1}^M N_j a_{j,i}^e \quad (24)$$

---

<sup>1</sup>In IFNO [15], only one Fourier layer is used iteratively (Fig. 4d). For convenience, when we say "The number of implicit Fourier layers is  $N$ ." or " $N$  implicit Fourier layers", we mean the number of iterations of the only Fourier layer in IFNO is  $N$ .

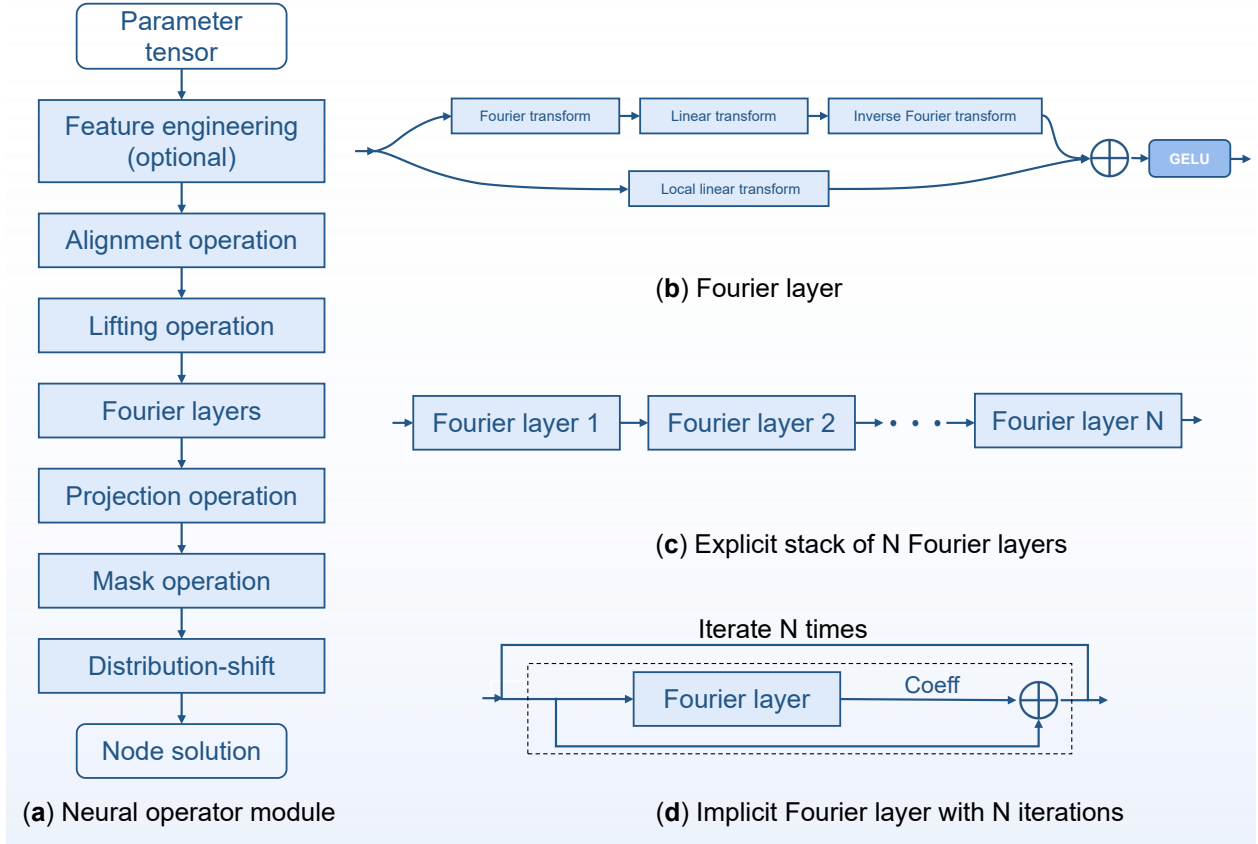


Figure 4: **Network details.** (a) The neural operator module in the VOL framework. Parameter tensor is fed into the neural operator module, after the feature engineering (optional) and a series of operations in the neural operator, the predicted node solution tensor is obtained. Then, the predicted node solution tensor is processed by the mask operation and the distribution-shift session to obtain the final output. (b) The Fourier layer used in all experiments of this paper. We do not filter out higher modes in Fourier layers as the original FNO [14] does. " $\oplus$ " denotes the element-wise addition operation between tensors. (c) Explicit stack of  $N$  Fourier layers. (d) Implicit Fourier layer with  $N$  iterations.

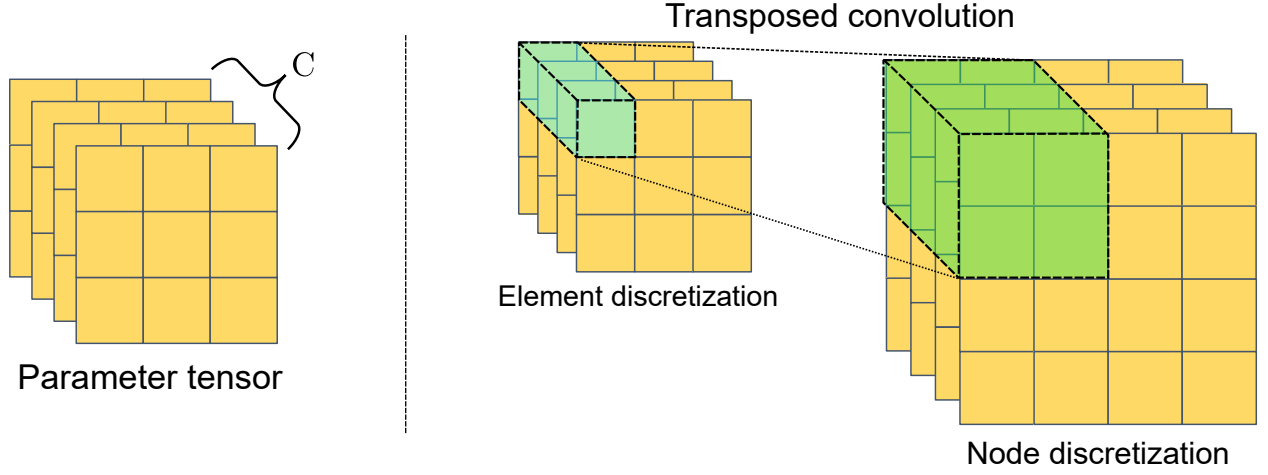


Figure 5: Left: The input parameter tensor contains  $C$  channels, each channel contains parameters at Gauss points of the same position of all elements, and  $C$  equals to the number of Gauss points in one element. Right:  $2 \times 2$  transposed convolution operation that transforms the parameter tensor discretized at elements into the tensor discretized at nodes.

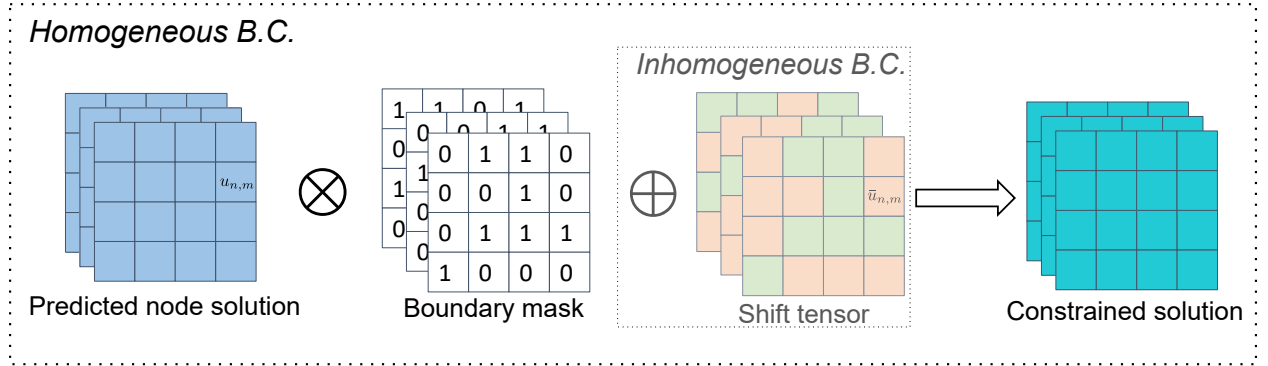


Figure 6: **Mask operation.** The homogeneous essential boundary conditions can be applied to the node solution by the mask operation (the element-wise product between the node solution and the mask tensor). " $\otimes$ " denotes the element-wise product between two tensors. The inhomogeneous boundary condition can be then applied with a shift tensor, where the red elements denote the inhomogeneous terms, and the green elements denote zeros. For example, as shown in the figure,  $u_{n,m}$  is the predicted solution to the  $n$ th degree of freedom of the  $m$ th node of the computational mesh, the corresponding element of which in the mask tensor is 0. And the corresponding element in the shift tensor is  $\bar{u}_{n,m}$ , which denotes the inhomogeneous term of the constraint of  $n$ th degree of freedom of  $m$ th node.

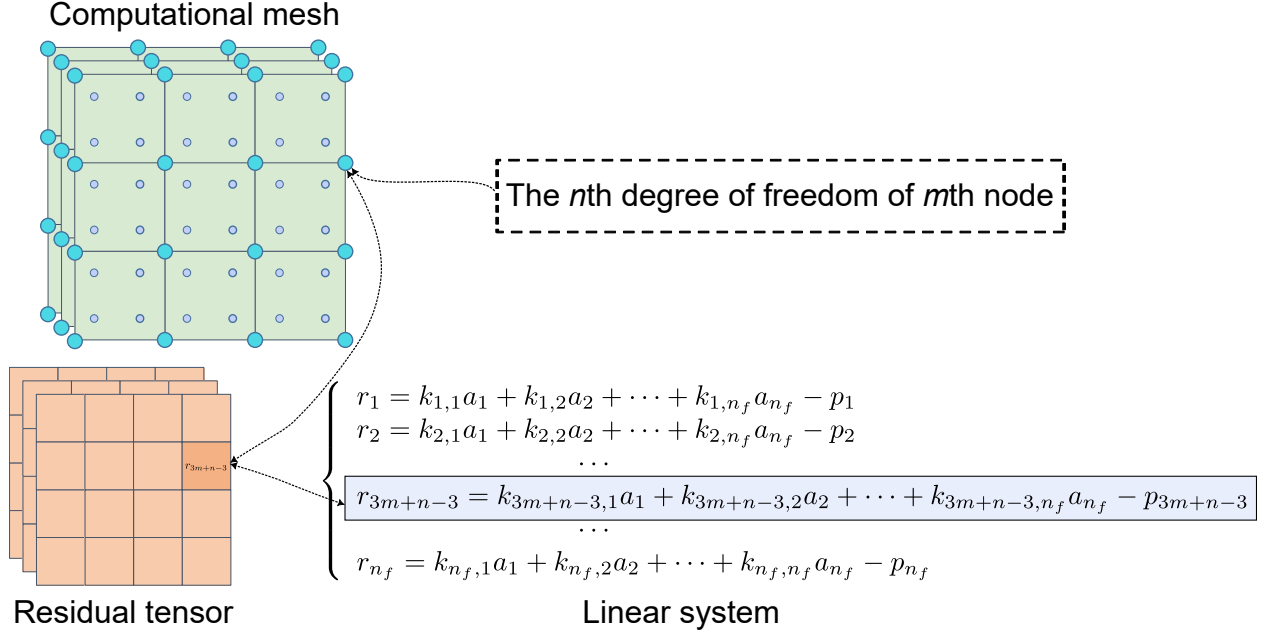


Figure 7: **The connection between the computational mesh, the residual tensor and the linear system.** Suppose that every node of the computational mesh has three degrees of freedom. The element  $r_{3m+n-3}$  of the residual tensor is just the residual of the  $(3m+n-3)$ th equation of the corresponding linear system.

and take the derivative of both sides

$$\frac{\partial u_i}{\partial \mathbf{x}} = \sum_{j=1}^M \mathbf{J}^{e-1} \frac{\partial N_j}{\partial \mathbf{r}} a_{j,i}^e \quad (25)$$

where  $M$  denotes the number of nodes of one element,  $a_{j,i}^e$  denotes the physical quantity of  $i$ th degree of freedom of  $j$ th node of the element<sup>2</sup>. These are essentially equivalent to a convolution operation on discrete node solution field, if the weight of the convolution filters is set as values of terms  $N_j$  and  $\mathbf{J}^{e-1} \frac{\partial N_j}{\partial \mathbf{r}}$  at Gauss points. On this basis, we develop the method of calculating Eq. 24 and Eq. 25 based on the standard non-trainable convolution operation, which can be implemented easily with tensor-based deep learning engines, as shown in Fig. 8A. In fact, similar tricks about convolution filters has been adopted by work [9], in which the weight of convolution filters are designed to conduct finite difference. In this paper, we use convolution to calculate weighted sum, which is a more general setting, that can not only be applied at Gauss points, but also can be applied anywhere else of the element domain in principle. Such way of weighted sum with convolution is well suited for the usage of isoparametric elements, that allow the elements that do not maintain orthogonality between the sides of the element.

(2) Calculate the integrand. In step (1), we get two types of weighted sum at Gauss points of all elements, i.e.,  $u_i$  and  $\frac{\partial u_i}{\partial x_j}$ , that gathered as tensors. In this step, as shown in Fig. 8B, these weighted sum tensors are first combined into quantities that have physical meaning, like the strain tensor  $\epsilon$ , to facilitate the calculation of integrand with Eq. 17. And then, the integrand is formed by calculating Eq. 17 with the combined tensor and tensors of parameters of PDEs. The process utilizes the idea of *domain knowledge embedding* in the section 2. Note that this step would be different in some implementation details with different governing equations. In this paper, steady heat transfer and elasticity are considered and implemented.

(3) Multiply Jacobian (Fig. 8C). The Jacobian tensor that contains the values of the Jacobian at Gauss

<sup>2</sup>Note  $\mathbf{a}^e$  is always treated as a vector conventionally. For example, if all nodes of the elements have three degree of freedom, then  $\mathbf{a}^e = [a_{1,1}^e, a_{1,2}^e, a_{1,3}^e, a_{2,1}^e, a_{2,2}^e, \dots, a_{M,1}^e, a_{M,2}^e, a_{M,3}^e]^T$ . To write  $a_{j,i}^e$  with two subscripts is just for convenience.

points of all elements is pre-computed, according to the configuration of all elements in the physical space. Then, the element-wise product of the integrand tensor and the Jacobian tensor are computed to obtain the integrand tensor that considers Jacobian effect.

(4) Calculate the functional approximation of the system with numerical integration (Fig. 8D). First, perform Gaussian quadrature for all elements, i.e., calculate weighted sum of the integrand by weight of Gauss points in every element. The element of result tensor is the functional approximation of the element  $\Pi^e$ . Then, sum up  $\Pi^e$  of all elements to get the functional approximation  $\tilde{\Pi}$ .

For line 6 of Algorithm 1, since the forward propagation from node solution to the functional has been constructed, the gradient of the functional to the node solution can be easily derived with automatic differentiation. A backward propagation from the functional to the node solution is conducted, to obtain the gradient of the functional with respect to the node solution, as shown in Fig. 8E. The gradient of the functional to the node solution is just the residual of the linear system, so it is denoted as the residual tensor  $\mathbf{R}$ .

As discussed above, from line 4 to line 6 of Algorithm 1, a forward-backward propagation loop between the node solution and the functional approximation has been constructed. The developed loop allows us to derive the residual of the linear system without acquiring element stiffness matrices and assembling the total stiffness matrix. The residual tensor  $\mathbf{R} = \frac{\partial \tilde{\Pi}}{\partial \mathbf{a}}$  is derived by just running the loop once, which has the same shape as the node solution. The element of the residual tensor is the just the residual of corresponding equation of the linear system Eq. 20, the same one that solved by FEMs, as shown in Fig. 7. Thus, the goal of the VOL (Eq. 22) has turned to solve all linear systems derived from the parameters of PDEs in the label-free training set. Note that the residual tensor  $\mathbf{R}$  now contains all residuals of the linear system. And we need to eliminate those elements in  $\mathbf{R}$  corresponding to variables that have been constrained, so that the coefficient matrix of the linear system is non-singular. Thus, an additional mask operation needs to be imposed on the residual tensor  $\mathbf{R}$  in line 7.

In this paper, we redevelop two common iteration methods, i.e., the steepest decent method (SD) and the conjugate gradient method (CG) with deep learning tensors to solve such linear systems. They are wrapped as two independent optimization strategies  $Opt$  used in line 8 of Algorithm 1. Instead of running all the iteration steps of SD or CG at once, we only use just one or several steps of these two iteration methods for one forward propagation, which is more computationally efficient and proves to be effective in our experiments (See section 4.). SD and CG with  $n$  steps update are shown in Algorithm 2 and Algorithm 3 respectively. They take all of the residual tensors of  $j$ th batch  $\mathbf{R}_j^{bs}$ , the prediction of current batch  $\mathbf{a}_j^{bs}$  and input parameter  $\mathbf{U}_j^{bs}$  as input, and return the update of current prediction  $\Delta \mathbf{a}_j^{bs}$ . To calculate  $\mathbf{R}^T \mathbf{K} \mathbf{R}$  in Algorithm 2 and  $\mathbf{p}^T \mathbf{K} \mathbf{p}$  in Algorithm 3, it is also unnecessary to obtain  $\mathbf{K}$ . All we need to do is to treat the residual tensor  $\mathbf{R}$  as the node-related quantity, and perform similar operations on  $\mathbf{R}$  as that in Fig. 8A-Fig. 8D, with a more simplified calculation than Eq. 17:

$$\begin{aligned} \mathbf{R}^T \mathbf{K} \mathbf{R} &= \sum_e \sum_{l=1}^{n_g} H_l \mathbf{R}^e \mathbf{B}_l^T \mathbf{D}_l \mathbf{B}_l \mathbf{R}^e |\mathbf{J}_l^e| \\ \mathbf{p}^T \mathbf{K} \mathbf{p} &= \sum_e \sum_{l=1}^{n_g} H_l \mathbf{p}^e \mathbf{B}_l^T \mathbf{D}_l \mathbf{B}_l \mathbf{p}^e |\mathbf{J}_l^e| \end{aligned} \quad (26)$$

Similarly, the forward-backward propagation loop can also be constructed between  $\mathbf{a}$  and  $\tilde{\Pi}_{temp}$  to derive the residual tensor of the next update step  $\mathbf{R}$  in line 10 of Algorithm 2, and between  $\mathbf{p}$  and  $\mathbf{p}^T \mathbf{K} \mathbf{p}$  to derive  $\mathbf{K} \mathbf{p}$  in line 9 of Algorithm 3. Then the same mask operation is also imposed on  $\mathbf{R}$  and  $\mathbf{p}^T \mathbf{K} \mathbf{p}$  respectively. Considering more steps of iteration methods will increase the computational cost, for all experiments in this work, when we use SD, we use only one step of SD in one inner loop in the VOL, and when we use CG, we use two steps of CG in one inner loop in the VOL.



With the update of current prediction  $\Delta \mathbf{a}_j^{bs}$ , we can manage to update the parameter  $\boldsymbol{\theta}$  of the neural operator module. Here, we adopt a simple way to derive the update of  $\boldsymbol{\theta}$ . First, we assume  $\mathbf{a}_j^{bs} + \Delta \mathbf{a}_j^{bs}$  to be a "provisional label" of the current batch. Then, we can define the loss metric that corresponds to the provisional label  $\hat{\mathbf{a}}_j^{bs} = \mathbf{a}_j^{bs} + \Delta \mathbf{a}_j^{bs}$  and the current prediction  $\mathbf{a}_j^{bs}$ , and we choose to use sum of squares error (SSE) as the loss metric:

$$\begin{aligned}\mathcal{L}_{\text{SSE}} &= \frac{1}{2} \text{sum} \left( \text{square} \left( \hat{\mathbf{a}}_j^{bs} - \mathbf{a}_j^{bs} \right) \right) \\ &= \frac{1}{2} \text{sum} \left( \text{square} \left( \left( \mathbf{a}_j^{bs} + \Delta \mathbf{a}_j^{bs} \right) - \mathbf{a}_j^{bs} \right) \right) \\ &= \frac{1}{2} \text{sum} \left( \text{square} \left( \Delta \mathbf{a}_j^{bs} \right) \right)\end{aligned}\tag{27}$$

Then in line 9 of Algorithm 1,  $\boldsymbol{\theta}$  is updated with the chain rule<sup>3</sup>

$$\begin{aligned}\boldsymbol{\theta} &= \boldsymbol{\theta} - \eta \cdot \text{einsum} \left( ' \cdots \mathbf{t}, \cdots \rightarrow \mathbf{t}', \text{grad} \left( \mathbf{a}_j^{bs}, \boldsymbol{\theta} \right), \text{grad} \left( \mathcal{L}_{\text{SSE}}, \mathbf{a}_j^{bs} \right) \right) \\ &= \boldsymbol{\theta} + \eta \cdot \text{einsum} \left( ' \cdots \mathbf{t}, \cdots \rightarrow \mathbf{t}', \text{grad} \left( \mathbf{a}_j^{bs}, \boldsymbol{\theta} \right), \Delta \mathbf{a}_j^{bs} \right)\end{aligned}\tag{28}$$

---

**Algorithm 2 Steepest descent** ( $n$  steps)

---

**Input:** residual tensor  $\mathbf{R}$ , current node solution  $\mathbf{a}$ , input parameter  $\mathbf{U}$ , mask operation  $Mask$

---

```

1:  $\mathbf{R} = -\mathbf{R}$ 
2:  $\Delta \mathbf{a} = \mathbf{0}$ 
3: for  $1 \leq i \leq n$  do
4:   Calculate  $\mathbf{R}^T \mathbf{K} \mathbf{R}$  corresponding to  $(\mathbf{U}, \mathbf{R})$ 
5:    $\alpha = \frac{\mathbf{R}^T \mathbf{R}}{\mathbf{R}^T \mathbf{K} \mathbf{R}}$ 
6:    $\Delta \mathbf{a} += \alpha \mathbf{R}$ 
7:   if  $n > 1$  then
8:      $\mathbf{a} += \alpha \mathbf{R}$ 
9:     Calculate  $\tilde{\Pi}_{temp}$  corresponding to  $(\mathbf{U}, \mathbf{a})$ 
10:     $\mathbf{R} = \frac{\partial \tilde{\Pi}_{temp}}{\partial \mathbf{a}}$ 
11:     $\mathbf{R} = Mask(\mathbf{R})$ 
12:     $\mathbf{R} = -\mathbf{R}$ 
13:   end if
14: end for
Return:  $\Delta \mathbf{a}$ 
```

---

<sup>3</sup>For convenience, we consider the all trainable parameters  $\boldsymbol{\theta}$  to form a vector.

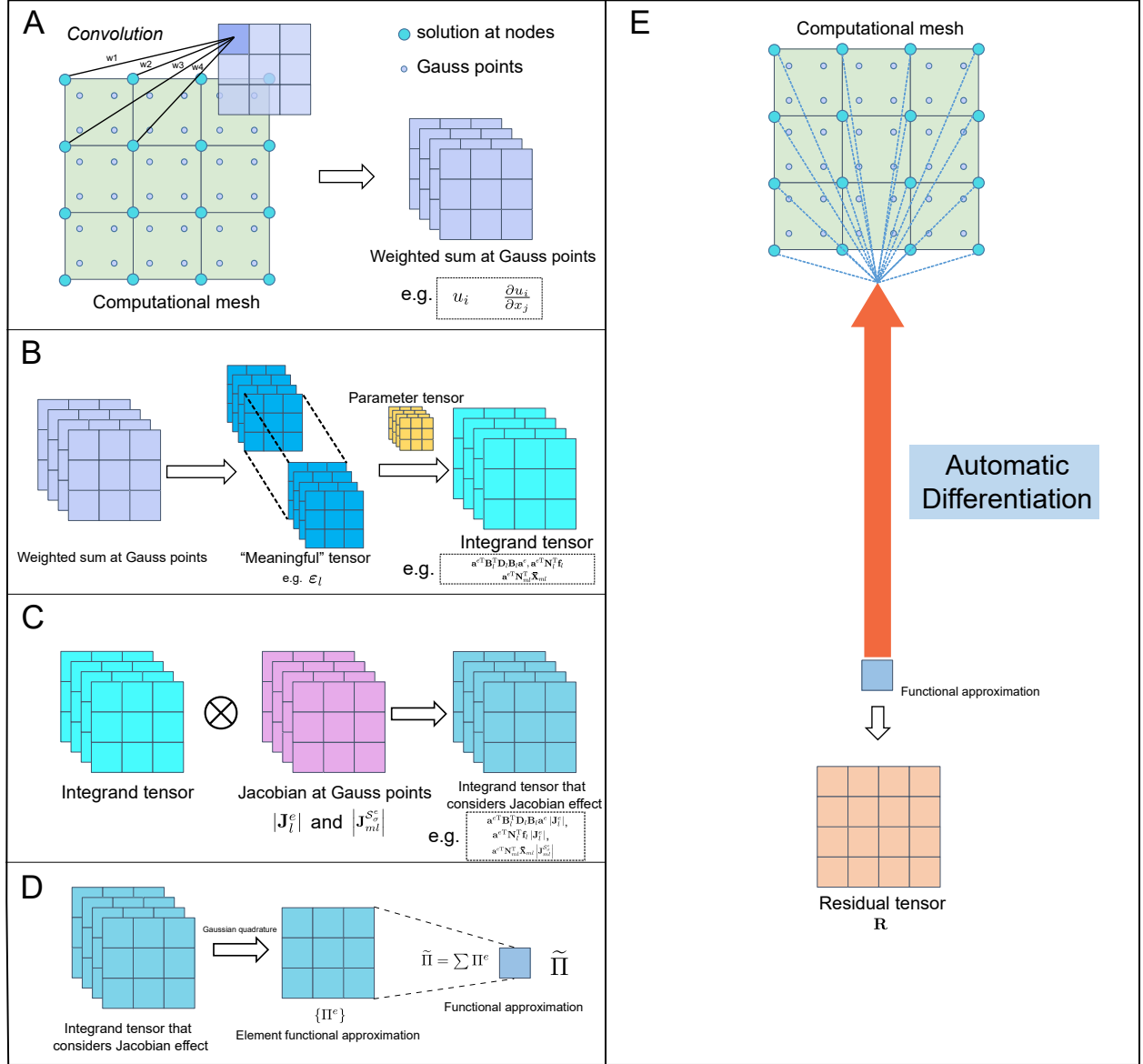


**Figure 8: Numerical integration implementation with the deep learning tensor operation and back-propagation.** Suppose we are handling a domain discretized by 9 quadrilateral elements with 4 nodes. **(A)** Evaluating weighted sum of node solution at Gauss points with the convolution. Note here only one component of node solution is plotted for simplicity, and calculation of more than one component may be needed in practice.  $w_1, w_2, w_3, w_4$  are pre-computed and fixed weight of convolution filters, according to the values of interpolation functions and their derivatives. The length, width and height of the 3D convolution filters and the width and height of the 2D convolution filters should be determined according to the shape of the element of computational mesh, and the number of the filters equals to the number of Gauss points in one element. In this illustration, the width $\times$ height of one filter is  $2\times 2$ , and 4 filters are needed. The shape of a weighted sum tensor is  $4\times 3\times 3$ . **(B)** Calculate the integrand of functional at Gauss points with the weighted sum and parameter tensor (e.g., element material property tensor, element thermal conductivity tensor) with Eq. 17. **(C)** Consider Jacobian effect on the integrand. A Jacobian tensor is constructed, with the same shape as the integrand, and then the element-wise product of the integrand tensor and the Jacobian tensor is calculated. **(D)** Gaussian quadrature to get tensor  $\{\Pi^e\}$  that has shape  $1\times 3\times 3$ , and sum up all elements of  $\{\Pi^e\}$  to obtain  $\Pi$ . **(E)** Backward propagation to implement Eq. 21.

---

**Algorithm 3 Conjugate gradient decent ( $n$  steps)**

---

**Input:** residual tensor  $\mathbf{R}$ , current node solution  $\mathbf{a}$ , input parameter  $\mathbf{U}$ , mask operation  $Mask$

```
1:  $\mathbf{R} = -\mathbf{R}$ 
2:  $\mathbf{p} = \mathbf{R}$ 
3:  $\Delta\mathbf{a} = \mathbf{0}$ 
4: for  $1 \leq i \leq n$  do
5:   Calculate  $\mathbf{p}^T \mathbf{K} \mathbf{p}$  corresponding to  $(\mathbf{U}, \mathbf{p})$ 
6:    $\alpha = \frac{\mathbf{R}^T \mathbf{R}}{\mathbf{p}^T \mathbf{K} \mathbf{p}}$ 
7:    $\Delta\mathbf{a} += \alpha \mathbf{p}$ 
8:   if  $n > 1$  then
9:      $\mathbf{K} \mathbf{p} = \frac{\partial(\mathbf{p}^T \mathbf{K} \mathbf{p})}{\partial \mathbf{p}}$ 
10:     $\mathbf{K} \mathbf{p} = Mask(\mathbf{K} \mathbf{p})$ 
11:     $\mathbf{R}_{new} = \mathbf{R} - \alpha \mathbf{K} \mathbf{p}$ 
12:     $\beta = \frac{\mathbf{R}_{new}^T \mathbf{R}_{new}}{\mathbf{R}^T \mathbf{R}}$ 
13:     $\mathbf{R} = \mathbf{R}_{new}$ 
14:     $\mathbf{p} = \mathbf{R} + \beta \mathbf{p}$ 
15:   end if
16: end for
Return:  $\Delta\mathbf{a}$ 
```

---

## 4 Results and discussion

In this section, we first investigate different optimization strategies for the VOL, and choose the setting of the section 4.2.1, 4.2.2, 4.3.1 and 4.3.2 depending on the results of the investigation. Then, in section 4.2.1, 4.2.2, 4.3.1 and 4.3.2, we demonstrate the capability of the proposed VOL for learning operators of the governing PDEs of steady heat transfer and variable stiffness elasticity. At last, we elaborate generalization benefits in the VOL from the perspective of neural solver, and observe the generalization benefits with experimental results. In the VOL, we keep the same mesh settings with the corresponding commercial FEM solvers. All experiments in this paper are implemented with Pytorch [34]. Code and datasets for all experiments in this paper will be published at this repository.

### 4.1 Investigation of different optimization strategies

In this section, we compare the effects of SD and CG with different number of explicit and implicit Fourier layers. The dataset used in this section is formally introduced in section 4.3.2. The common settings of these experiments in this section are shown in Table 2.

Size of label-free training set	Size of shift set	Size of test set
1000	10	100
Learning rate	Batch size	Number of epochs
1	1	200

Table 2: Common settings for experiments in section 4.1.

From Table 3, we observe CG has a relative  $L_2$  error on test set 17.0%-25.6% smaller than SD in all experiments, while SD is more time-saving, costs 12.2%-21.3% less time than CG. E4 has the smallest

	E4	I4	I6
SD	93.28/6.13/5369	125.11/9.04/5363	123.80/8.85/6690
CG	91.73/4.56/6826	127.70/7.50/6620	126.92/7.21/7933
	I8	I10	
SD	122.55/8.71/8836	121.56/8.61/10330	
CG	125.60/7.09/10128	124.53/7.01/11764	

Table 3: **Average  $L_2$  norm of the residual tensor of the training set (N) at the final epoch of training, average relative  $L_2$  error of test set (%) and training cost (s) of experiments with different optimization strategies and different layer settings.** Column: E4: 4 explicit Fourier layers, I4: 4 implicit Fourier layers, I6: 6 implicit Fourier layers, I8: 8 implicit Fourier layers, I10: 10 implicit Fourier layers. Cell: Average  $L_2$  norm of the residual tensor of the training set at the final epoch, average relative  $L_2$  error (%) of test set and training cost in seconds (s) are in order from left to right in a cell.

	E4	I4	I6	I8	I10
Forward/backward pass size (MB)	18.21	18.21	24.44	30.67	36.90
Params size (MB)	67.25	16.87	16.87	16.87	16.87
Estimated total size (MB)	85.49	35.11	41.34	47.57	53.80
Model weight (MB)	64.15	16.09	16.09	16.09	16.09

Table 4: Model summaries of memory consumption different layer settings.

relative  $L_2$  test error among all layer settings. From I4 to I10, the relative  $L_2$  error on test set is getting lower as the number of implicit layers increases, but still higher than E4, and the training time cost is also getting higher. The model weights of all experiments are saved in `pth` format. The model weights of E4 takes up 64.15 MB of disk space, while I4, I6, I8 and I10 take only 16.09 MB. More detailed model summaries are listed in Table 4. Considering time cost and consumption of memory, we choose the setting of I4+CG for experiments of all benchmark problems in section 4.2.1, 4.2.2, 4.3.1, and 4.3.2. In these sections, we use more unlabeled data for training, and larger labeled test dataset to validate the effectiveness of the proposed VOL. Results of these sections show that the VOL can give solutions with a reasonable accuracy with enough unlabeled data, as shown in Table 5 and Table 6. All experiments in these sections are based on the architecture illustrated in Fig. 4. For elasticity problems, two same neural operators are used to predict displacement in  $x$  and  $y$  directions respectively, each of them is based on Fig. 4 with a single channel of output. Unless otherwise stated, all experiments in these sections and the section 4.4 use the following settings:

- (1) Four implicit Fourier layers are used, the width of Fourier layer is 32, and the number of origin modes and the number of transformed modes of Fourier layer are both 16.
- (2) Alignment operation is implemented with a  $2 \times 2$  transposed convolution, padding size is 0, and stride is 1.
- (3) Lifting operation: A linear layer maps the input to 32 channels.
- (4) Projection operation uses such a sequence: Linear layer maps 32 channels to 128 channels - GELU [35] activation function - Linear layer maps 128 channels to 1 channel (output channel).
- (5) Learning rate is set to 1, and batch size is set to 1. Number of epochs is 500.

(6) Data type is float64.

	Size of label-free training set	Size of test set	Size of shift set
§4.2.1	9490	500	10
§4.2.2	10000	2000	10
§4.3.1	12000	2000	5
§4.3.2	12000	2000	5

Table 5: Size of training set, test set, and shift set of experiments in section 4.2.1, 4.2.2, 4.3.1 and 4.3.2.

	Average $L_2$ norm (W/ (m · K))	Average relative $L_2$ error (%)
§4.2.1	2.52 E-3	1.34
§4.2.2	3.56 E-3	2.20
	Average $L_2$ norm (N)	Average relative $L_2$ error (%)
§4.3.1	39.54	1.58
§4.3.2	55.46	2.93

Table 6: Average  $L_2$  norm of the residual tensor of the training set at the final epoch of training and average relative  $L_2$  error of test set.

## 4.2 Steady heat transfer

In this section, the performance of VOL on 2D steady heat transfer problems is investigated. The governing equation of 2D steady heat transfer problems is described as

$$\frac{\partial}{\partial x} \left( \kappa_x(x, y) \frac{\partial T(x, y)}{\partial x} \right) + \frac{\partial}{\partial y} \left( \kappa_y(x, y) \frac{\partial T(x, y)}{\partial y} \right) + Q(x, y) = 0, \quad (29)$$

$$(x, y) \in [0, 1\text{m}] \times [0, 1\text{m}]$$

where  $T$  represents temperature,  $\kappa_x(x, y)$ ,  $\kappa_y(x, y)$  represent thermal conductivity in x and y direction, and  $Q(x, y)$  is source term. Two cases are considered: (1)  $\kappa_x = \kappa_y = \kappa(x, y)$  is a function of coordinates x and y, while  $Q$  is constant; (2)  $\kappa_x = \kappa_y$  is constant and  $Q$  is a function of coordinates x and y. The goal of the VOL is to learn the mapping between the thermal conductivity (or heat source) parameter space and the temperature space. Real temperature solution field minimizes the following functional:

$$I = \frac{1}{2} \int_{\Omega} \left[ \kappa_x \left( \frac{\partial T}{\partial x} \right)^2 + \kappa_y \left( \frac{\partial T}{\partial y} \right)^2 - 2QT \right] d\Omega \quad (30)$$

The way to approximate Eq. 30 is the same as the process of elaborated in the section 3.2 and 3.3. We first calculate the temperature gradient  $\nabla T = \left[ \frac{\partial T}{\partial x}, \frac{\partial T}{\partial y} \right]^T$  and  $QT$  at Gauss points with weighted sum of the temperature node solution, and with tensor operations, we can easily derive the approximation  $\tilde{I}$  of the system functional  $I$ . Then, by the variational operation that implemented by automatic differentiation, we can derive the residual tensor.

For both cases, the 4-node bilinear quadrilateral element is used for meshing, the mesh size is  $30 \times 30$ , and all temperature labels for the test and the distribution-shift session of the output are generated with the commercial software COMSOL [36]. In the VOL, we use the bilinear quadrilateral element to mesh the domain. The shape of the parameter tensor (the thermal conductivity tensor in section 4.2.1 and the heat source tensor in section 4.2.2) is  $4 \times 30 \times 30$ . The shape of the node solution tensor (the temperature tensor) is  $1 \times 31 \times 31$ .

#### 4.2.1 Case 1: constant source term and variable thermal conductivity

A unit square domain OACB with various types of boundary conditions is considered, as shown in the left figure of Fig. 9. OA, AC, CE, DB and BO are adiabatic boundaries, and DE is a Dirichlet boundary with  $T = 0$ . Variable thermal conductivity field  $\kappa(\mathbf{x}) = \kappa(x, y)$  is implemented with Gaussian random field generated with the Karhunen–Loève expansion:

$$\begin{aligned}\kappa(\mathbf{x}) &\sim \mathcal{GP}(1.5, k_l(\mathbf{x}, \mathbf{x}')) \text{ W/(m} \cdot \text{K)} \\ k_l(\mathbf{x}, \mathbf{x}') &= \sigma e^{-\frac{\|\mathbf{x}-\mathbf{x}'\|^2}{2l^2}} \text{ W/(m} \cdot \text{K)}\end{aligned}\tag{31}$$

where  $l = \frac{1}{2}$ ,  $\sigma = \frac{1}{6}$ . Heat source is set as  $1 \text{ W/m}^2$ . Representative samples and their corresponding results of this case are shown in Fig. 10 and Fig. 11.

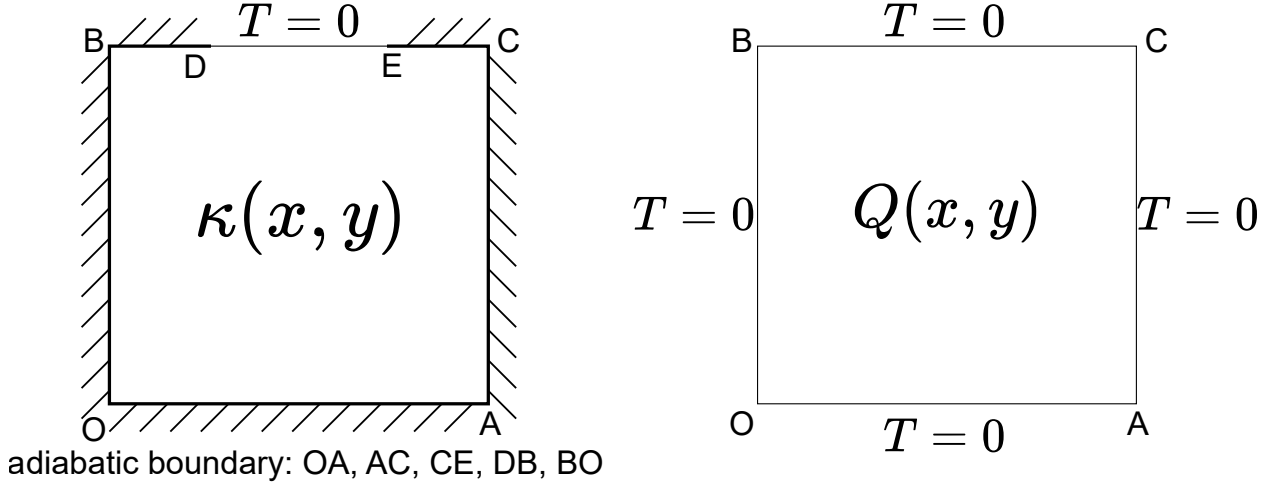


Figure 9: **Geometry and boundary conditions of 2D steady heat transfer problems.** Left (case1): The solution domain OACB is a unit square.  $OA=AC=BO=1\text{m}$ ,  $DB=CE=\frac{4}{15}\text{m}$ , and  $DE=\frac{7}{15}\text{m}$ . OA, AC, CE, DB and BO are adiabatic boundaries, and DE is a Dirichlet boundary with  $T = 0$ . Right (case2): The solution domain OACB is also a  $1\text{m} \times 1\text{m}$  unit square. All boundaries are Dirichlet boundaries with  $T = 0$ .

#### 4.2.2 Case 2: constant thermal conductivity and variable source term

In this case, all boundaries set as Dirichlet boundaries  $T = 0$ , as shown on the right of Fig. 9. Thermal conductivity is set as  $0.01 \text{ W/(m} \cdot \text{K)}$ . Heat source  $Q(\mathbf{x}) = Q(x, y)$  is also implemented with Gaussian random field generated with the Karhunen–Loève expansion:

$$\begin{aligned}Q(\mathbf{x}) &\sim \mathcal{GP}(0, k_l(\mathbf{x}, \mathbf{x}')) \text{ W/m}^2 \\ k_l(\mathbf{x}, \mathbf{x}') &= \sigma e^{-\frac{\|\mathbf{x}-\mathbf{x}'\|^2}{2l^2}} \text{ W/m}^2\end{aligned}\tag{32}$$

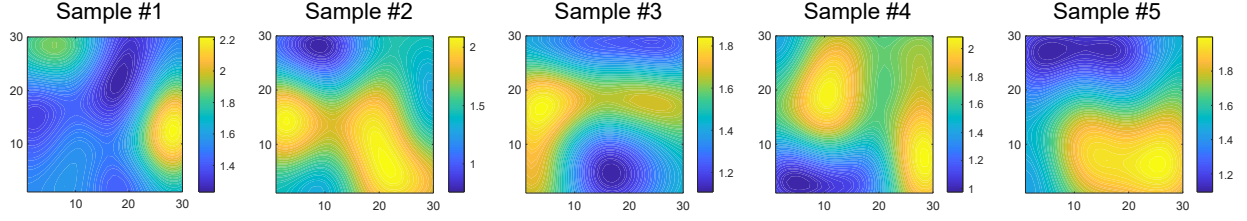


Figure 10: **Thermal conductivity  $\kappa(x, y)$  ( $\text{W}/(\text{m} \cdot \text{K})$ ) of the five random samples in the test dataset of Case 1 (constant thermal conductivity and variable source term) of the 2D steady heat transfer problems.** Each sample has one column. The results of these five samples are shown in Fig. 11.

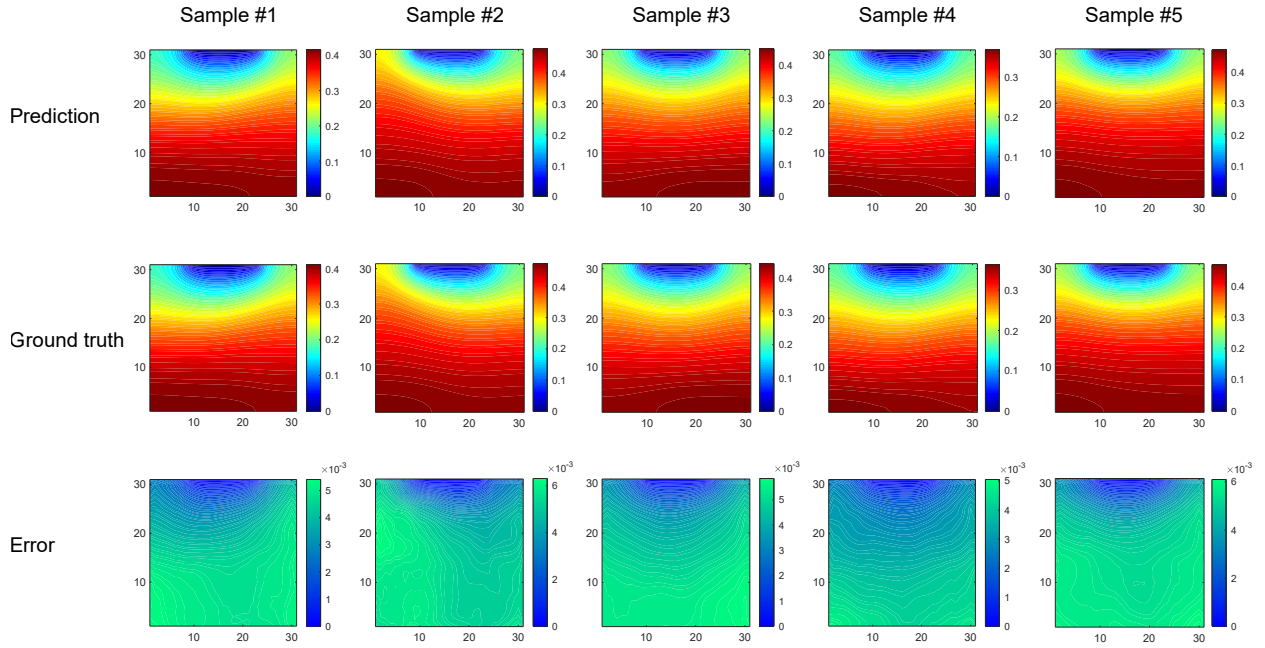


Figure 11: **Representative results for Case 1 (constant source term and variable thermal conductivity) of the 2D steady heat transfer problems of five random samples in test dataset.** Each sample has one column. First row: prediction of temperature ( $^{\circ}\text{C}$ ) solution of the five random samples by the VOL. Second row: labels of temperature ( $^{\circ}\text{C}$ ) solution of the five random samples. Third row: the absolute error ( $^{\circ}\text{C}$ ) of five random samples.

where  $l = \frac{1}{2}, \sigma = 1$ .

In this section, we use a different experiment setting from other sections. The main reason is that we observe learning rate 1.0 and batch size 1 lead to explosion results (The output of neural operators explode to NaN.). So, we decrease the learning rate to  $1e^{-5}$ , and increase the batch size to 64 for this case. The number of epochs is 5000. Besides, the architecture of the neural operator is also a bit different. For the alignment operation, we use the  $2 \times 2$  convolution operation with no padding and unit stride to adjust the feature map from the element discretization to the size of inner nodes, and apply a unit zero padding to the output, so that the output is at the size of the node discretization. The mode of Fourier layers is set as 14. Representative samples and their corresponding results of this case are shown in Fig. 12 and Fig. 13.

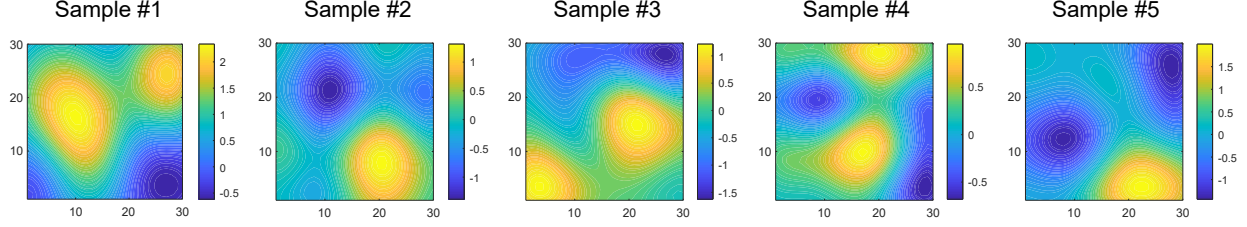


Figure 12: **Heat source  $Q(x, y)$  ( $\text{W}/\text{m}^2$ ) of the five random samples in the test dataset of Case 2 (constant thermal conductivity and variable source term) of the 2D steady heat transfer problems.** Each sample has one column. The results of these five samples are shown in Fig. 13.

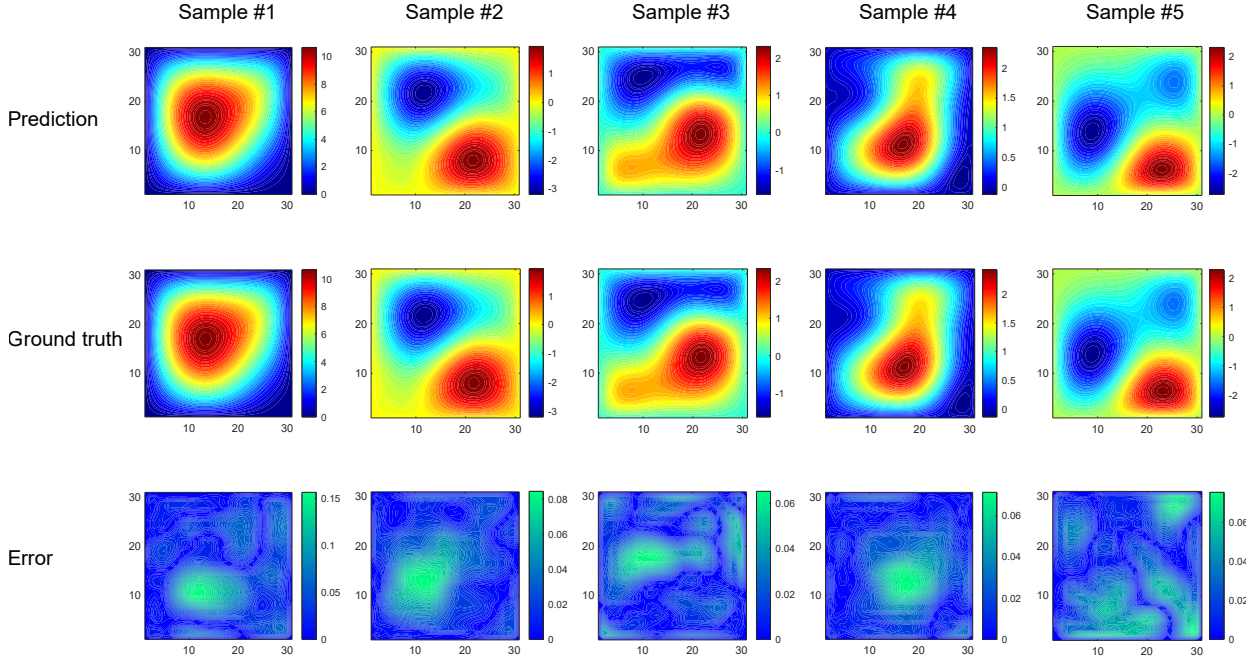


Figure 13: **Representative results for Case 2 (constant thermal conductivity and variable source term) of the 2D steady heat transfer problems of five random samples in test dataset.** Each sample has one column. First row: prediction of temperature ( $^{\circ}\text{C}$ ) solution of the five random samples by the VOL. Second row: labels of temperature ( $^{\circ}\text{C}$ ) solution of the five random samples. Third row: the absolute error ( $^{\circ}\text{C}$ ) of five random samples.



### 4.3 Variable stiffness elasticity

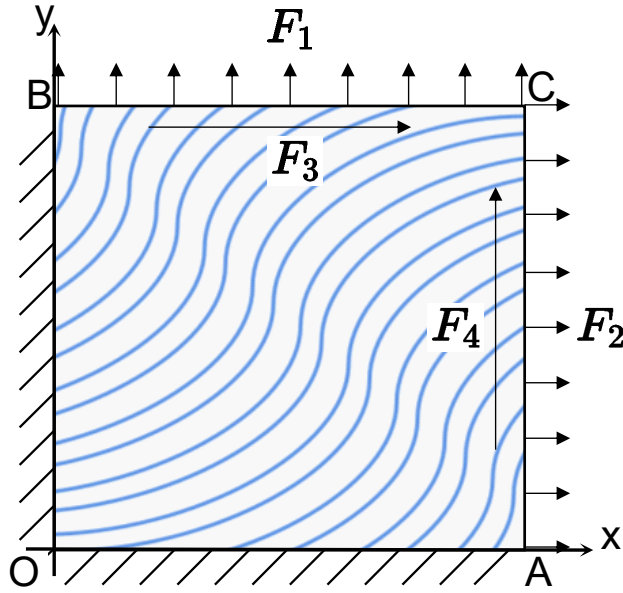


Figure 14: **Geometry and boundary conditions of variable stiffness elasticity problems.** A fiber-reinforced panel OACB is considered.  $OA=AC=CB=BO=100\text{mm}$ , OA and OB are displacement boundaries with  $u_1 = u_2 = 0$ , AC and CB are traction boundaries.  $F_1$  and  $F_3$  are line loads applied on boundary BC.  $F_2$  and  $F_4$  are line loads applied on boundary AC.  $F_1=5 \text{ N/mm}$ ,  $F_3=5*x \text{ N/mm}$ ,  $F_2=5 \text{ N/mm}$  and  $F_4=5*y \text{ N/mm}$ . The variation of fiber angle leads to variable stiffness property.

An elastic variable stiffness square plate with in-plane deformation is investigated in this section, and it is considered to be made of the fiber reinforced material, as shown in Fig. 14. The thickness of the plate is  $0.125\text{mm}$ . Due to spatial variation of fiber orientation, the material property of the plate shows anisotropy. The material property matrix in x-y coordinate system  $\mathbf{C}_{xy}$  can be written as:

$$\mathbf{C}_{xy} = \mathbf{T}^{-1} \mathbf{C}_{12} \mathbf{T}^{-T} \quad (33)$$

where

$$\mathbf{T} = \begin{bmatrix} \cos^2 \theta & \sin^2 \theta & 2 \sin \theta \cos \theta \\ \sin^2 \theta & \cos^2 \theta & -2 \sin \theta \cos \theta \\ -\sin \theta \cos \theta & \sin \theta \cos \theta & \cos^2 \theta - \sin^2 \theta \end{bmatrix} \quad (34)$$

And  $\mathbf{C}_{12}$  is the material property matrix in the principle material coordinates, which is not effected by the fiber angle. Eq. 35 gives the formulation of compliance matrix  $\mathbf{S}_{12}$ , i.e., the inverse of  $\mathbf{C}_{12}$ :

$$\mathbf{S}_{12} = \begin{bmatrix} \frac{1}{E_1} & -\frac{\nu_{12}}{E_1} & 0 \\ -\frac{\nu_{12}}{E_1} & \frac{1}{E_2} & 0 \\ 0 & 0 & \frac{1}{G_{12}} \end{bmatrix} \quad (35)$$

We first calculate  $\mathbf{S}_{12}$ , then calculate the inverse of  $\mathbf{S}_{12}$  to derive  $\mathbf{C}_{12}$ .

According to [37], AS4/3501-6 is chosen as the material of the plate. Mechanical properties of AS4/3501-6 used in this paper are given in Table 7. In this section, the fiber angle field  $\theta = \theta(x, y)$  of the plate is characterized in two ways: (1) Linear 1-D variation. (2) B-splines surface. These two ways with their results

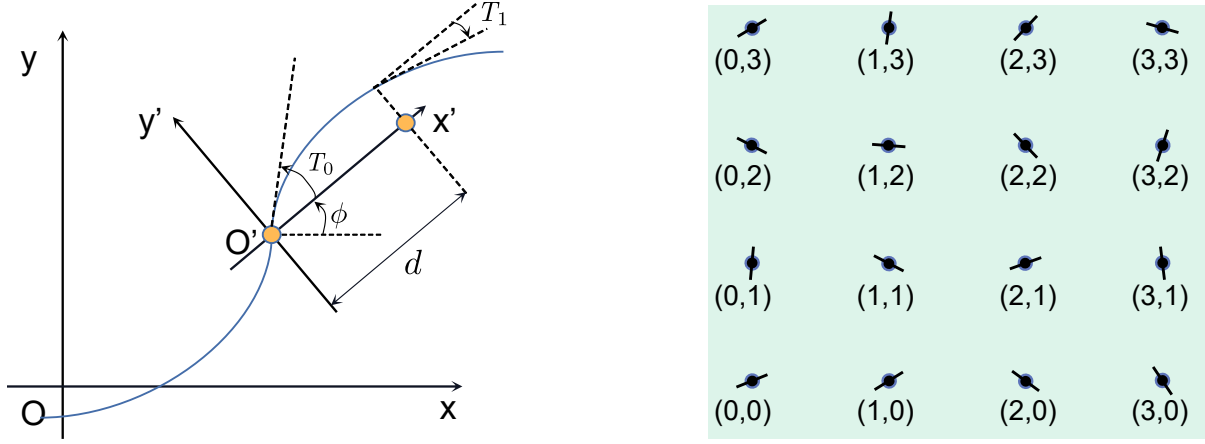


Figure 15: Left: Variation of the fiber orientation. Right:  $4 \times 4$  control points with random angle values.

are discussed separately in the section 4.3.1 (case 1) and section 4.3.2 (case 2). The boundary conditions of both cases are same, as shown in Fig. 14. The goal of the VOL is to learn the mapping between the fiber angle field space and the vector space of displacement components  $[u_1, u_2]^T$ . In this paper, two neural operators are used to learn  $u_1$  and  $u_2$  separately. As a simple feature engineering,  $\sin \theta$ ,  $\cos \theta$ ,  $\sin 2\theta$ ,  $\cos 2\theta$  are fed to neural operators, rather than  $\theta$  itself.

For both cases, displacement labels for the test and the distribution-shift of output are generated with ABAQUS [38]. The S4R shell element is used for meshing, the mesh size is  $32 \times 32$ . In the VOL, we use the bilinear quadrilateral element with reduced integration to mesh the plate. The shape of the parameter tensor (angle field tensor) is  $1 \times 32 \times 32$ . The shape of the node solution tensor (the displacement tensor) is  $2 \times 33 \times 33$ .

Table 7: Mechanical properties of AS4/3501-6 [37] used in this paper.

$E_1$ (MPa)	$E_2$ (MPa)	$\nu_{12}$	$G_{12}$ (MPa)
126000	11000	0.28	6600

#### 4.3.1 Case 1: Linear 1-D variation

According to [39, 40], the fiber orientation angle along a reference path takes the form

$$\theta(x') = \phi + (T_1 - T_0) \frac{|x'|}{d} + T_0 \quad (36)$$

where  $\phi$  is the angle of rotation of the new coordinate system  $x'-O'-y'$  with respect to the original coordinate system  $x-O-y$ .  $x'$  is the  $x'$  coordinate in coordinate system  $x'-O'-y'$ ,  $L$  denotes the side length of the plate,  $T_0$  is the fiber orientation angle according to  $x'$  axis at the panel center,  $T_1$  is the fiber orientation angle according to  $x'$  axis at  $x' = \pm d$ , as shown on the left of Fig. 15. In this case,  $d$  is set as half of the side length of the panel. The fiber angle fields can then be sampled by sampling  $\phi$ ,  $T_0$  and  $T_1$ . In this case, we use Latin hypercube sampling (LHS) to sample the tuple  $(\phi, T_0, T_1)$ . The bounds of  $\phi$ ,  $T_0$  and  $T_1$  are all set as  $(-\frac{1}{2}\pi, \frac{1}{2}\pi)$ . Total  $1e^5$  tuples of  $(-\frac{1}{2}\pi, \frac{1}{2}\pi)$  are sampled for this case, and only the first 12005 samples are utilized for the generation of angle fields. Then the angle fields are split for training, testing and distribution-shift session, as shown in Table 5. Representative samples and their corresponding results of this case are shown in Fig. 16, Fig. 17, and Fig. 18.

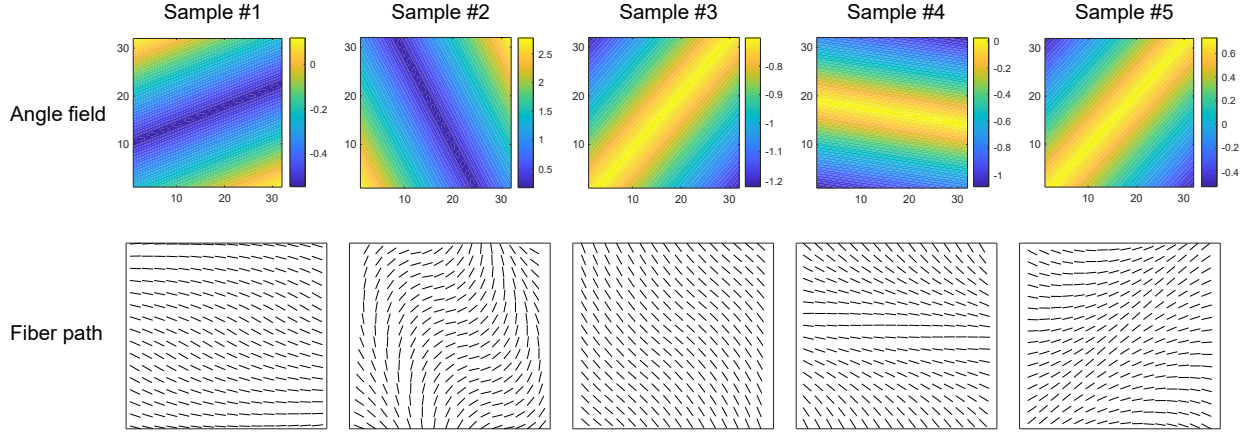


Figure 16: **The angle field  $\theta(x, y)$  and corresponding fiber path of five random samples in test dataset of Case 1 (Linear 1-D variation) of variable stiffness elasticity problems.** Each sample has one column. First row: angle field  $\theta(x, y)$  (rad) of the five random samples. Second row: the fiber path of the five random samples. The results of displacement in x and y directions of these five samples are shown in Fig. 17 and Fig. 18 respectively.

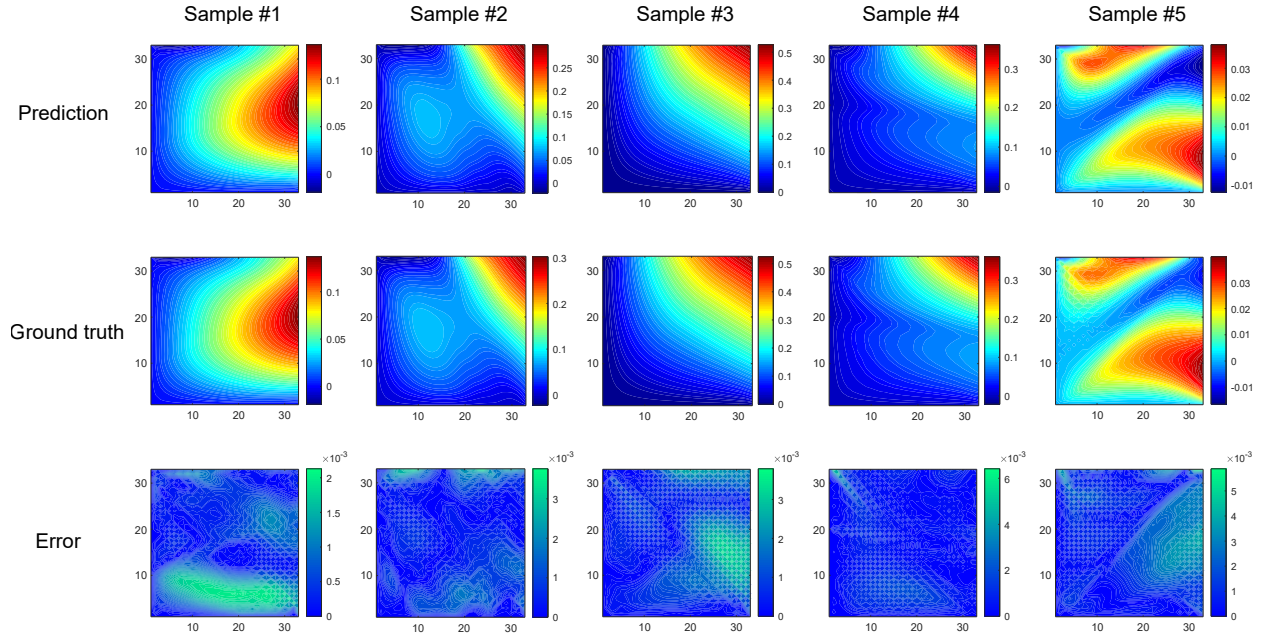


Figure 17: **Representative results of displacement in x direction for Case 1 (Linear 1-D variation) of variable stiffness elasticity problems of five random samples in test dataset.** Each sample has one column. First row: prediction of displacement in x direction (mm) of the five random samples by the VOL. Second row: labels of displacement in x direction (mm) of the five random samples by the VOL. Third row: the absolute error (mm) of five random samples.

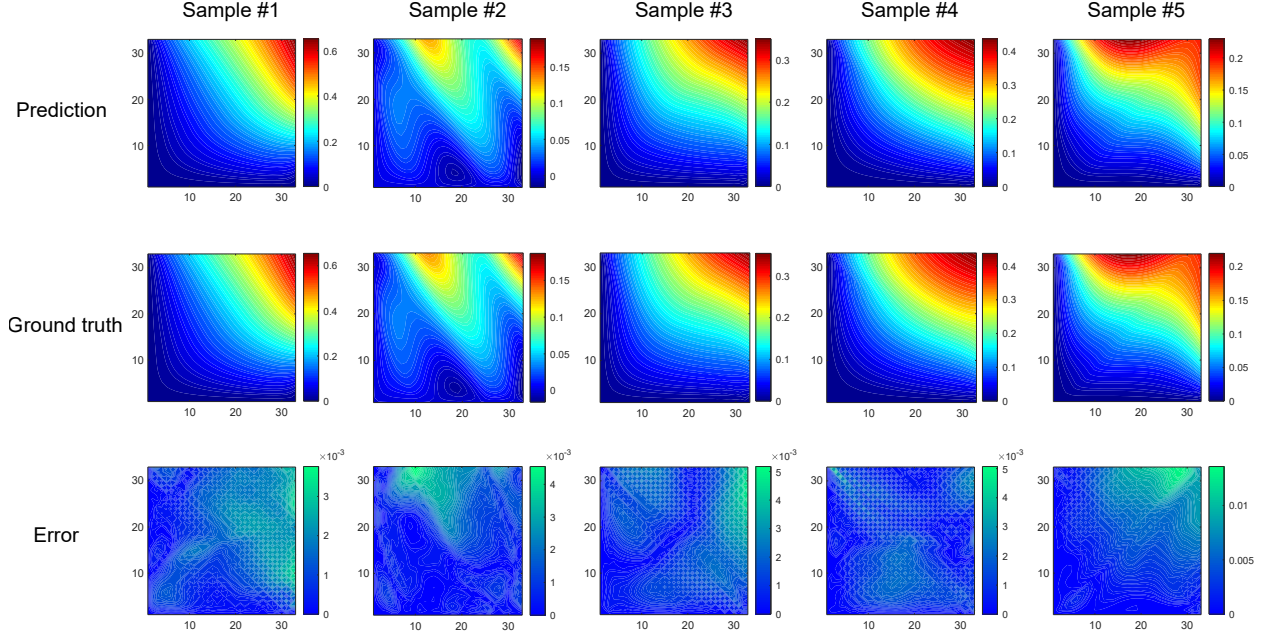


Figure 18: **Representative results of displacement in y direction for Case 1 (Linear 1-D variation) of variable stiffness elasticity problems of five random samples in test dataset.** Each sample has one column. First row: prediction of displacement in y direction (mm) of the five random samples by the VOL. Second row: labels of displacement in y direction (mm) of the five random samples by the VOL. Third row: the absolute error (mm) of five random samples.

#### 4.3.2 Case 2: B-Splines surface

Following [41], the fiber angle fields can be characterized by the idea of the B-Splines. The B-Splines surface representation [42] is:

$$\mathbf{S}(u, v) = \sum_{i=0}^n \sum_{j=0}^m N_{i,p}(u) N_{j,q}(v) \mathbf{P}_{i,j} \quad (37)$$

where  $N_{i,p}(u)$  and  $N_{j,q}(v)$  denote basis functions along u direction and v direction respectively,  $\mathbf{P}_{i,j}$  denotes coordinates of control points. In this case, a linear mapping between the physics coordinates  $(x, y)$  and the parameter coordinates  $(u, v)$  is defined:

$$u = \frac{x}{L}, v = \frac{y}{L} \quad (38)$$

The control points of the B-spline are equally spaced in the x and y directions. We just fix all  $x$  and  $y$  coordinates of control points, and keep the  $z$  coordinates active. We do not use the actual B-spline surface to characterize the angle field. Instead, the fiber angle field is treated as the  $z$  axis component  $Z(x_p, y_p)$  of the B-Splines surface. For a specific position  $(x_p, y_p)$  of the plate, the parameter coordinates of which are  $(u_p, v_p)$ , we have the fiber angle  $\theta(x_p, y_p)$  at the position  $(x_p, y_p)$

$$\theta(x_p, y_p) = Z(x_p, y_p) = \sum_{i=0}^n \sum_{j=0}^m N_{i,p}(u_p) N_{j,q}(v_p) Z_{i,j} \quad (39)$$

Thus, the fiber angle fields can be sampled by sampling the  $z$  coordinates of all control points. In this case,  $m = n = 3$ ,  $p = 2$ , i.e., a  $4 \times 4$  mesh of control points and 2nd-degree B-spline basis functions are used.

The control points are illustrated on the right of Fig. 15. We use LHS to sample the  $z$  coordinates of all control points, and all bounds of the  $z$  coordinates of all control points are set as  $(-\frac{1}{2}\pi, \frac{1}{2}\pi)$ . Representative samples and their corresponding results of this case are shown in Fig. 19, Fig. 20, and Fig. 21.

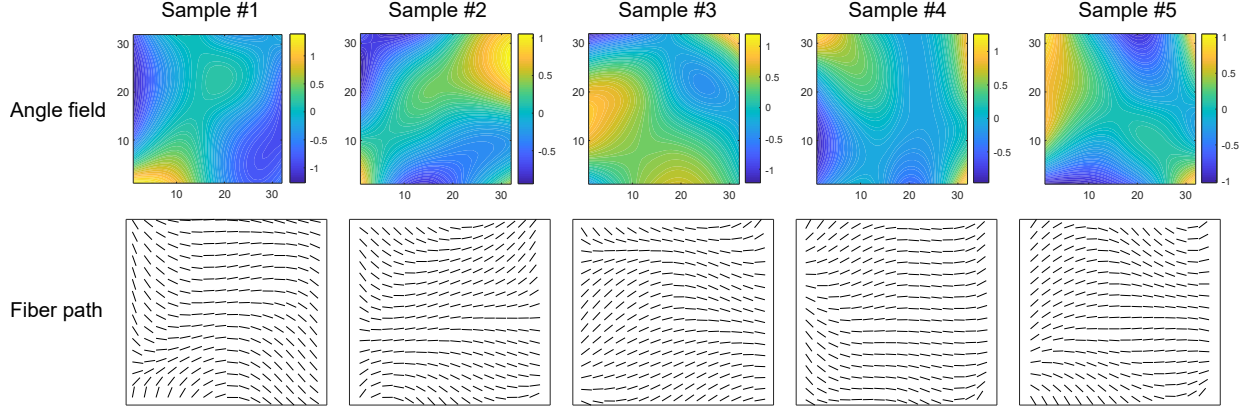


Figure 19: **The angle field  $\theta(x, y)$  and corresponding fiber path of five random samples in test dataset of Case 2 (B-Splines surface) of variable stiffness elasticity problems.** Each sample has one column. First row: angle field  $\theta(x, y)$  (rad) of the five random samples. Second row: the fiber path of the five random samples. The results of displacement in  $x$  and  $y$  directions of these five samples are shown in Fig. 20 and Fig. 21 respectively.

#### 4.4 Generalization benefits

From the perspective of the neural solver, the *generalization*, as the unique advantage of the machine learning, especially of the deep learning, can be utilized to provide better initial solutions for the solver solving new problems. In this section, we demonstrate that the generalization of neural operators brings a huge boost to the performance of the solvers. We reuse the data with 2000 instances of section 4.3.2. To validate the power of the generalization of neural operators in the framework of the VOL, we design four independent experiments, of which the first two contain the different conventional solvers without neural operators, and the second two contain the whole process of the VOL, with neural operators and different solvers: (1) (Experiment SD.) Use the SD as solver, without neural solvers, to solve all instances one by one. (2) (Experiment CG.) Use the CG as solver, without neural solvers, to solve all instances one by one. (3) (Experiment VOL+SD.) The VOL with the SD solver. (4) (Experiment VOL+CG.) The VOL with the CG solver. The common settings of experiments (3) and (4) are listed in Table 8. For one instance of the dataset, (1) and (2) run exactly the same number of the iterations (The number is 500.) as the epochs of (3) and (4). Note that for comparison, we keep all settings of the solvers same for (1) and (3), (2) and (4) respectively. So the CG in (2) just actually updates two steps of the conjugate gradient method in one iteration, and start another new update for the next iteration. For every epoch and iteration of the whole dataset, we record the mean relative  $L_2$  error of the whole dataset of the four experiments and plot them in Fig. 22. We observe the VOL+SD and VOL+CG are an order of magnitude smaller than SD and CG respectively. The mean relative  $L_2$  error of SD and CG at the final iteration, VOL+SD and VOL+CG at the final epoch are 1.03 and 0.70, 5.57 E-2 and 4.50 E-2 respectively, as shown in Table 9. The mean relative  $L_2$  error of SD without the neural operator is 18.49 times higher than VOL+SD with the same solver setting. For CG, the number is 15.56. The performance gain comes from the generalization of the neural operators. The neural operators keep learning and provide more accurate initial solution for the solver, thus improving the performance. In fact, if we treat the neural operators in the framework of VOL as the deep models embedded in the classical iteration solvers, then the



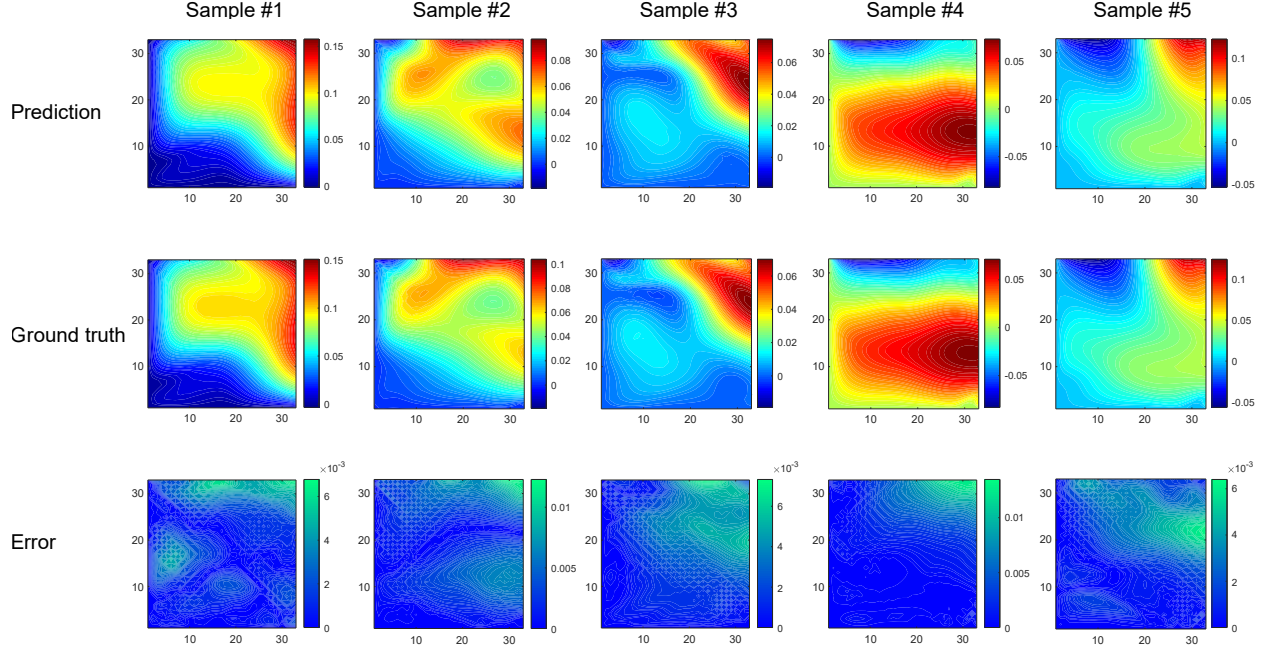


Figure 20: **Representative results of displacement in x direction for Case 2 (B-Splines surface) of variable stiffness elasticity problems of five random samples in test dataset.** Each sample has one column. First row: prediction of displacement in x direction (mm) of the five random samples by the VOL. Second row: labels of displacement in x direction (mm) of the five random samples by the VOL. Third row: the absolute error (mm) of five random samples.

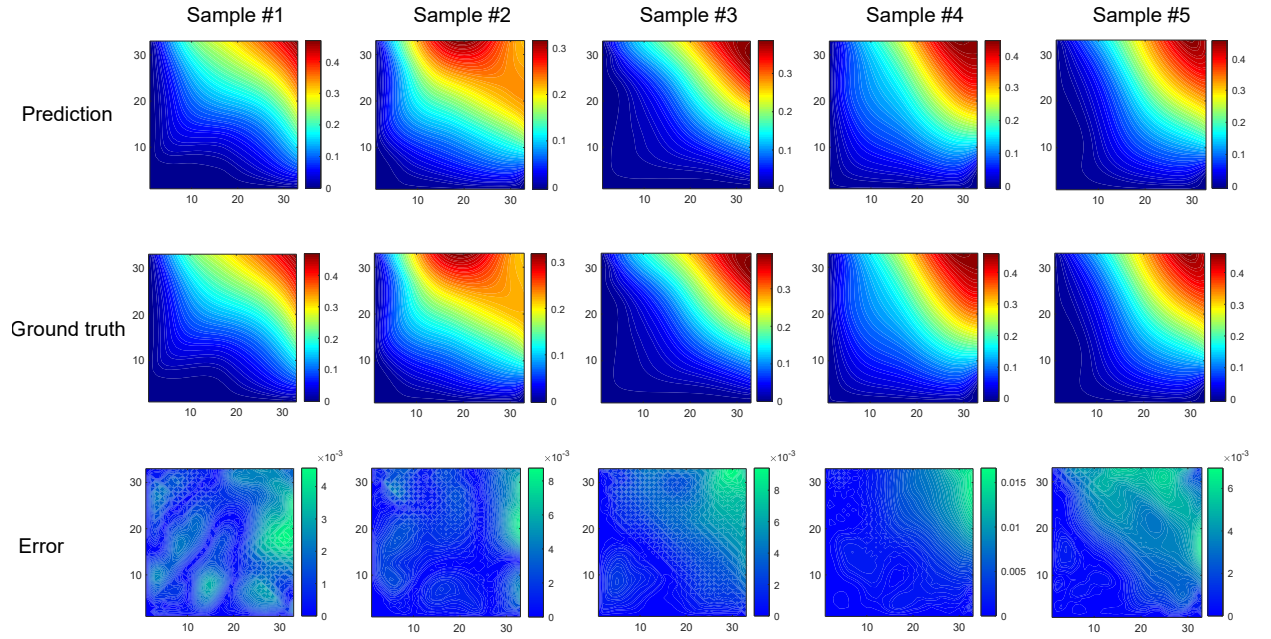


Figure 21: **Representative results of displacement in y direction for Case 2 (B-Splines surface) of variable stiffness elasticity problems of five random samples in test dataset.** Each sample has one column. First row: prediction of displacement in y direction (mm) of the five random samples by the VOL. Second row: labels of displacement in y direction (mm) of the five random samples by the VOL. Third row: the absolute error (mm) of five random samples.

VOL can also be categorized as the deep model embedding approach referred in section 2.

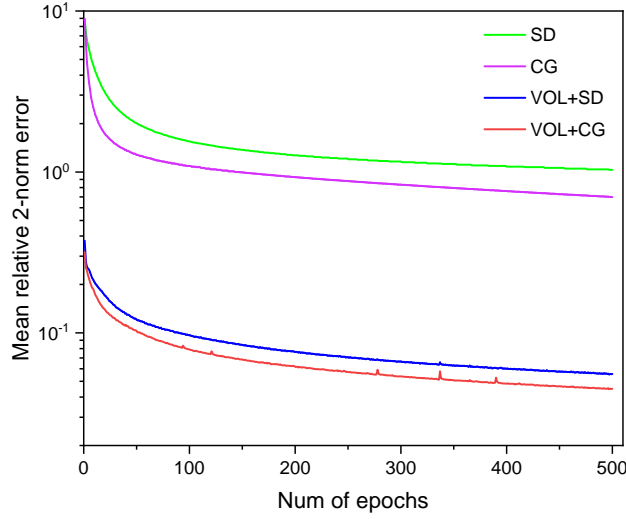


Figure 22: Mean relative  $L_2$  error of the training set of four experiments in the section 4.4.

Data size	Learning rate	Batch size	Number of epochs	Size of shift set
2000	1	1	500	5

Table 8: Common settings of the VOL used in experiments of section 4.4.

Experiments	SD	VOL+SD	CG	VOL+CG
Mean relative $L_2$ error	103%	5.57%	70%	4.50%
Ratio	18.49		15.56	

Table 9: **Results of four experiments of section 4.4.** The second row: the mean relative  $L_2$  error at the final iteration of the four experiments. The third row: the ratio of the mean relative  $L_2$  error at the final iteration of SD and CG with their VOL counterparts.

## 5 Conclusion and outlook

Both the conventional solver and the data-driven surrogate modeling have their own merits and shortcomings. The conventional solvers, that are based on the domain knowledge, can give reliable solutions to a wide variety of PDEs, and the conventional solvers are affordable when dealing with a single instance of PDEs or small number of samples, but they often have low efficiency and bring a heavy computational burden when the mass sampling of parameters of PDEs is required. On the contrary, the data-driven surrogate modeling can give reasonable prediction of solutions to a range of parameters with a fast inference speed. However, as mentioned in Introduction (See section 1.), the data-driven surrogate modeling needs a data preparation stage and a model training stage, which are isolated from each other. The access to substantial labeled data and the training process bring also quite a computational burden to the data-driven surrogate modeling. Moreover,

the data-driven nature of training process may lead to unreliability of the inference solution given by the trained surrogate model. In this work, a novel paradigm that has the merits of both and complements the shortcomings has been proposed, which we refer to as the variational operator learning (VOL). The proposed VOL first uses the node output of neural operators to approximate functional of the system, and then uses the backpropagation from the functional to the node output to derive the residual tensor, finally uses optimization strategies to minimize the residual tensor. Specifically, we redevelop the SD and the CG, two most common iteration methods to solve linear systems, to give the neural operators a cheap yet effective update for every iteration step. We first compare different optimization strategies of the VOL with the different layer settings. We observe CG performs better than SD on all layer settings, while also takes a bit longer time. We then conduct experiments of steady heat transfer and variable stiffness elasticity. For all cases in section 4.2 and 4.3, the VOL can achieve satisfactory results with small error, as long as enough cheap unlabeled data are provided. The VOL is essentially solving all linear systems of training set simultaneously, while utilizing the information of solving process to update parameters of the neural operator after every iteration step. We propose that, in the framework of VOL, the neural operators can give better and better initial solution for the SD and the CG in every iteration, benefiting from generalization. We observe the generalization of neural operators can reduce the mean relative  $L_2$  error by an order of magnitude.

Many interesting aspects for the proposed VOL can be explored in the future work. First, we do not know theoretically yet how to find the best experimental settings of the VOL to a specific problem. A certain combination of the batch size and learning rate may lead to the result explosion on some problems, while not on others. Developing a theory to determine the best experimental settings is challenging yet vital for practical application of the proposed VOL. Second, the VOL itself can be improved. More kinds of loss metrics can be explored in the parameters update procedure of the VOL. Besides, other neural architectures and more powerful optimization strategies can be integrated into the VOL. Third, applying the VOL to downstream applications, such as inverse problems, control and optimization. Fourth, some techniques may be developed to eliminate the output distribution-shift session, making the VOL label-free completely. Fifth, the VOL may be adapted so that it can be extended to nonlinear and dynamic systems. Sixth, the idea of the VOL could inspire new label-efficient designs for surrogate models other than neural operators.

## 6 Acknowledgments

This work was supported by National Key Research and Development Program of China (2021YFF0306404), and National Natural Science Foundation of China (U21A20429).

## References

- [1] Wing Kam Liu, Shaofan Li, and Harold S Park. Eighty years of the finite element method: Birth, evolution, and future. *Archives of Computational Methods in Engineering*, pages 1–23, 2022.
- [2] Robert Eymard, Thierry Gallouët, and Raphaële Herbin. Finite volume methods. *Handbook of numerical analysis*, 7:713–1018, 2000.
- [3] Randall J LeVeque. *Finite difference methods for ordinary and partial differential equations: steady-state and time-dependent problems*. SIAM, 2007.
- [4] Guirong Liu. *Meshfree methods: moving beyond the finite element method*. CRC press, 2009.
- [5] Weinan E and Bing Yu. The deep ritz method: A deep learning-based numerical algorithm for solving variational problems. *Communications in Mathematics and Statistics*, 6:1–12, 3 2018.



- [6] Justin Sirignano and Konstantinos Spiliopoulos. DGM: A deep learning algorithm for solving partial differential equations. *Journal of Computational Physics*, 375:1339–1364, 12 2018.
- [7] Maziar Raissi, Paris Perdikaris, and George Em Karniadakis. Physics-informed neural networks: A deep learning framework for solving forward and inverse problems involving nonlinear partial differential equations. *Journal of Computational Physics*, 378:686–707, 02 2019.
- [8] E. Samaniego, C. Anitescu, S. Goswami, V.M. Nguyen-Thanh, H. Guo, K. Hamdia, X. Zhuang, and T. Rabczuk. An energy approach to the solution of partial differential equations in computational mechanics via machine learning: Concepts, implementation and applications. *Computer Methods in Applied Mechanics and Engineering*, 362:112790, 04 2020.
- [9] Han Gao, Luning Sun, and Jian Xun Wang. PhyGeoNet: Physics-informed geometry-adaptive convolutional neural networks for solving parameterized steady-state pdes on irregular domain. *Journal of Computational Physics*, 428, 3 2021.
- [10] Rishikesh Ranade, Chris Hill, and Jay Pathak. DiscretizationNet: A machine-learning based solver for navier–stokes equations using finite volume discretization. *Computer Methods in Applied Mechanics and Engineering*, 378, 5 2021.
- [11] Sifan Wang, Hanwen Wang, and Paris Perdikaris. Learning the solution operator of parametric partial differential equations with physics-informed DeepONets. *Science Advances*, 7, 10 2021.
- [12] Zongyi Li, Hongkai Zheng, Nikola Kovachki, David Jin, Haoxuan Chen, Burigede Liu, Kamyar Azizzadenesheli, and Anima Anandkumar. Physics-informed neural operator for learning partial differential equations. *arXiv preprint arXiv:2111.03794*, 11 2021.
- [13] N. Sukumar and Ankit Srivastava. Exact imposition of boundary conditions with distance functions in physics-informed deep neural networks. *Computer Methods in Applied Mechanics and Engineering*, 389:114333, 2022.
- [14] Zongyi Li, Nikola Kovachki, Kamyar Azizzadenesheli, Burigede Liu, Kaushik Bhattacharya, Andrew Stuart, and Anima Anandkumar. Fourier neural operator for parametric partial differential equations. *arXiv preprint arXiv:2010.08895*, 2020.
- [15] Huaqian You, Quinn Zhang, Colton J. Ross, Chung-Hao Lee, and Yue Yu. Learning deep implicit fourier neural operators (IFNOs) with applications to heterogeneous material modeling. *Computer Methods in Applied Mechanics and Engineering*, 398:115296, 08 2022.
- [16] Jan S Hesthaven, Gianluigi Rozza, Benjamin Stamm, et al. *Certified reduced basis methods for parametrized partial differential equations*, volume 590. Springer, 2016.
- [17] Michael Eldred, Anthony Giunta, and S Collis. Second-order corrections for surrogate-based optimization with model hierarchies. In *10th AIAA/ISSMO multidisciplinary analysis and optimization conference*, page 4457, 2004.
- [18] Zhenguo Nie, Haoliang Jiang, and Levent Burak Kara. Stress field prediction in cantilevered structures using convolutional neural networks. *Journal of Computing and Information Science in Engineering*, 20, 2 2020.
- [19] Haoliang Jiang, Zhenguo Nie, Roselyn Yeo, Amir Barati Farimani, and Levent Burak Kara. StressGAN: A generative deep learning model for two-dimensional stress distribution prediction. *Journal of Applied Mechanics, Transactions ASME*, 88, 5 2021.

- [20] Zongyi Li, Nikola Kovachki, Kamyar Azizzadenesheli, Burigede Liu, Kaushik Bhattacharya, Andrew Stuart, and Anima Anandkumar. Neural operator: Graph kernel network for partial differential equations. *arXiv preprint arXiv:2003.03485*, 2020.
- [21] Lu Lu, Pengzhan Jin, Guofei Pang, Zhongqiang Zhang, and George Em Karniadakis. Learning nonlinear operators via DeepONet based on the universal approximation theorem of operators. *Nature Machine Intelligence*, 3:218–229, 3 2021.
- [22] Burr Settles. Active learning literature survey. Computer Sciences Technical Report 1648, University of Wisconsin–Madison, 2009.
- [23] Houpu Yao, Yi Gao, and Yongming Liu. FEA-Net: A physics-guided data-driven model for efficient mechanical response prediction. *Computer Methods in Applied Mechanics and Engineering*, 363:112892, 5 2020.
- [24] Juncai He and Jinchao Xu. MgNet: A unified framework of multigrid and convolutional neural network. *Science China Mathematics*, 62:1331–1354, 05 2019.
- [25] Alex Krizhevsky and Geoffrey E. Hinton. Learning multiple layers of features from tiny images. Technical report, Department of Computer Science, University of Toronto, 2009.
- [26] Jiequn Han, Linfeng Zhang, Roberto Car, and Weinan E. Deep Potential: A general representation of a many-body potential energy surface. *Communications in Computational Physics*, 23, 2018.
- [27] Mengcheng Huang, Zongliang Du, Chang Liu, Yonggang Zheng, Tianchen Cui, Yue Mei, Xiao Li, Xiaoyu Zhang, and Xu Guo. Problem-independent machine learning (PIML)-based topology optimization—a universal approach. *Extreme Mechanics Letters*, 56, 10 2022.
- [28] Hong Wu Zhang, Jing Kai Wu, Jun Lü, and Zhen Dong Fu. Extended multiscale finite element method for mechanical analysis of heterogeneous materials. *Acta Mechanica Sinica/Lixue Xuebao*, 26:899–920, 12 2010.
- [29] Ayano Kaneda, Osman Akar, Jingyu Chen, Victoria Kala, David Hyde, and Joseph Teran. A deep conjugate direction method for iteratively solving linear systems. *arXiv preprint arXiv:2205.10763*, 5 2022.
- [30] Chen Cui, Kai Jiang, Yun Liu, and Shi Shu. Fourier neural solver for large sparse linear algebraic systems. *arXiv preprint arXiv:2210.03881*, 10 2022.
- [31] Tianping Chen and Hong Chen. Approximation capability to functions of several variables, nonlinear functionals, and operators by radial basis function neural networks. *IEEE Transactions on Neural Networks*, 6(4):904–910, 1995.
- [32] Tianping Chen and Hong Chen. Universal approximation to nonlinear operators by neural networks with arbitrary activation functions and its application to dynamical systems. *IEEE Transactions on Neural Networks*, 6(4):911–917, 1995.
- [33] Luning Sun, Han Gao, Shaowu Pan, and Jian-Xun Wang. Surrogate modeling for fluid flows based on physics-constrained deep learning without simulation data. *Computer Methods in Applied Mechanics and Engineering*, 361:112732, 04 2020.

- [34] Adam Paszke, Sam Gross, Francisco Massa, Adam Lerer, James Bradbury, Gregory Chanan, Trevor Killeen, Zeming Lin, Natalia Gimelshein, Luca Antiga, Alban Desmaison, Andreas Kopf, Edward Yang, Zachary DeVito, Martin Raison, Alykhan Tejani, Sasank Chilamkurthy, Benoit Steiner, Lu Fang, Junjie Bai, and Soumith Chintala. PyTorch: An imperative style, high-performance deep learning library. In *Advances in Neural Information Processing Systems* 32, pages 8024–8035. Curran Associates, Inc., 2019.
- [35] Dan Hendrycks and Kevin Gimpel. Bridging nonlinearities and stochastic regularizers with gaussian error linear units. *arXiv preprint arXiv:1606.08415*, 2016.
- [36] COMSOL. <http://www.comsol.com/products/multiphysics/>.
- [37] A. S. Kaddour, M. J. Hinton, P. A. Smith, and S. Li. Mechanical properties and details of composite laminates for the test cases used in the third world-wide failure exercise. *Journal of Composite Materials*, 47:2427–2442, 9 2013.
- [38] ABAQUS. <https://www.3ds.com/products-services/simulia/products/abaqus/>.
- [39] Zafer Gürdal and Reynaldo Olmedo. In-plane response of laminates with spatially varying fiber orientations: Variable stiffness concept. *AIAA Journal*, 31:751–758, 1993.
- [40] Zafer Gürdal, Brian. F. Tatting, and C. K. Wu. Variable stiffness composite panels: Effects of stiffness variation on the in-plane and buckling response. *Composites Part A: Applied Science and Manufacturing*, 39:911–922, 5 2008.
- [41] Kunpeng Zhang, Dachuan Liu, Qun Wang, Peng Hao, Yuhui Duan, Hao Tang, and Bo Wang. Multi-level intelligent design of variable angle tow laminates via image-driven method. *Composite Structures*, 303, 1 2023.
- [42] Les Piegl and Wayne Tiller. *The NURBS book*. Springer, 1997.